

# Molecular diffusion of stable water isotopes in polar firn as a proxy for past temperatures

Christian Holme<sup>†\*a</sup>, Vasileios Gkinis<sup>\*a</sup>, and Bo M. Vinther<sup>a</sup>

<sup>a</sup>The Niels Bohr Institute, Centre for Ice and Climate, Juliane Maries Vej 30, 2100  
Copenhagen, Denmark

<sup>†</sup>Corresponding author: christian.holme@nbi.ku.dk (C. Holme)

<sup>\*</sup>The two authors contributed equally to this work

## Abstract

Polar precipitation archived in ice caps contains information on past temperature conditions. Such information can be retrieved by measuring the water isotopic signals of  $\delta^{18}\text{O}$  and  $\delta\text{D}$  in ice cores. These signals have been attenuated during densification due to molecular diffusion in the firn column, where the magnitude of the diffusion is isotopologue specific and temperature dependent. By utilizing the differential diffusion signal, dual isotope measurements of  $\delta^{18}\text{O}$  and  $\delta\text{D}$  enable multiple temperature reconstruction techniques. This study assesses how well six different methods can be used to reconstruct past surface temperatures from the diffusion-based temperature proxies. Two of the methods are based on the single diffusion lengths of  $\delta^{18}\text{O}$  and  $\delta\text{D}$ , three of the methods employ the differential diffusion signal, while the last uses the ratio between the single diffusion lengths. All techniques are tested on synthetic data in order to evaluate their accuracy and precision. We perform a benchmark test to thirteen high resolution Holocene data sets from Greenland and Antarctica, which represent a broad range of mean annual surface temperatures and accumulation rates. Based on the benchmark test, we comment on the accuracy and precision of the methods. Both the benchmark test and the synthetic data test demonstrate that the most precise reconstructions are obtained when using the single isotope diffusion lengths, with precisions of approximately  $1.0^\circ\text{C}$ . In the benchmark test, the single isotope diffusion lengths are also found to reconstruct consistent temperatures with a root-mean-square-deviation of  $0.7^\circ\text{C}$ . The techniques employing the differential diffusion signals are more uncertain, where the most precise method has a precision of  $1.9^\circ\text{C}$ . The diffusion length ratio method is the least precise with a precision of  $13.7^\circ\text{C}$ . The absolute temperature estimates from this method are also shown to be highly sensitive to the choice of fractionation factor parameterization.

## Keywords

Holocene, paleoclimatology, ice cores, isotope geochemistry, stable isotopes, diffusion, Greenland, Antarctica.

## 1 INTRODUCTION

Polar precipitation stored for thousands of years in the ice caps of Greenland and Antarctica contains unique information on past climatic conditions. The isotopic composition of polar ice, commonly expressed through the  $\delta$  notation has been used as a direct proxy of the relative depletion of a water vapor mass in its journey from the evaporation site to the place where condensation takes place (Epstein et al. 1951, Mook 2000). Additionally, for modern times, the isotopic signal of present day shows a good correlation with the temperature of the cloud at the time of precipitation (Dansgaard 1954, 1964) and as a result it has been proposed and used as a proxy of past temperatures (Jouzel & Merlivat 1984, Jouzel et al. 1997, Johnsen et al. 2001).

The use of the isotopic paleothermometer presents some notable limitations. The modern day linear relationship between  $\delta^{18}\text{O}$  and temperature commonly referred to as the “spatial slope” may hold for present conditions, but studies based on borehole temperature reconstruction (Cuffey et al. 1994, Johnsen et al. 1995) as well as the thermal fractionation of the  $\delta^{15}\text{N}$  signal in polar firn (Severinghaus et al. 1998, Severinghaus & Brook 1999) have independently underlined the inaccuracy of the spatial isotope slope when it is extrapolated to past climatic conditions. Even though qualitatively the  $\delta^{18}\text{O}$  signal comprises past temperature information, it fails to provide a quantitative picture on the magnitudes of past climatic changes.

Johnsen (1977), Whillans & Grootes (1985) and Johnsen et al. (2000) set the foundations for the quantitative description of the diffusive processes the water isotopic signal undergoes in the porous firn layer from the time of deposition until pore close-off. Even though the main purpose of Johnsen et al. (2000) was to investigate how to reconstruct the part of the signal that was attenuated during the diffusive processes, the authors make a reference to the possibility of using the assessment of the diffusive rates as a proxy for past firn temperatures.

The temperature reconstruction method based on isotope firn diffusion requires data of high resolution. Moreover, if one would like to look into the differential diffusion signal, datasets of both  $\delta^{18}\text{O}$  and  $\delta\text{D}$  are required. Such data sets have until recently not been easy to obtain especially due to the challenging nature of the  $\delta\text{D}$  analysis (Bigeleisen et al. 1952, Vaughn et al. 1998). With the advent of present commercial high-accuracy, high-precision Infra-Red spectrometers (Crosson 2008, Brand et al. 2009), simultaneous measurements of  $\delta^{18}\text{O}$  and  $\delta\text{D}$  have become easier to obtain. Coupling of these instruments to Continuous Flow Analysis systems (Gkinis et al. 2011, Maselli et al. 2013, Emanuelsson et al. 2015,

Jones et al. 2017) can also result in measurements of ultra-high resolution, a necessary condition for accurate temperature reconstructions based on water isotope diffusion.

A number of existing works have presented past firn temperature reconstructions based on water isotope diffusion. Simonsen et al. (2011) and Gkinis et al. (2014) used high resolution isotopic datasets from the NorthGRIP ice core (NGRIP members 2004). The first study makes use of the differential diffusion signal, utilizing spectral estimates of high-resolution dual  $\delta^{18}\text{O}$  and  $\delta\text{D}$  datasets covering the GS-1 and GI-1 periods in the NorthGRIP ice core (Rasmussen et al. 2014). The second study presents a combined temperature and accumulation history of the past 16,000 years based on the power spectral density (**PSD** hereafter) signals of high resolution  $\delta^{18}\text{O}$  measurements of the NorthGRIP ice core. More recently, van der Wel et al. (2015) introduced a slightly different approach for reconstructing the differential diffusion signal and testing it on dual  $\delta^{18}\text{O}$ ,  $\delta\text{D}$  high resolution data from the EDML ice core (Oerter et al. 2004). By artificially forward-diffusing the  $\delta\text{D}$  signal the authors estimate differential diffusion rates by maximizing the correlation between the  $\delta^{18}\text{O}$  and  $\delta\text{D}$  signal. In this work we attempt to test the various approaches in utilizing the temperature reconstruction technique.

We use synthetic, as well as real ice core data sets that represent Holocene conditions from a variety of drilling sites on Greenland and Antarctica. Our objective is to use data sections that originate from parts of the core as close to present day as possible. By doing this we aim to minimize possible uncertainties and biases in the ice flow thinning adjustment that is required for temperature interpretation of the diffusion rate estimates. Such a bias has been shown to exist for the NorthGRIP ice core (Gkinis et al. 2014), most likely due to the Dansgaard & Johnsen (1969) ice flow model overestimating the past accumulation rates for the site. In order to include as much data as possible, approximately half of the datasets used here have an age of 9-10 ka. This age coincides with the timing of the early Holocene Climate Optimum around 5-9 ka (**HCO** hereafter). For Greenlandic drill sites, temperatures were up to 3°C warmer than present day during the HCO (Dahl-Jensen et al. 1998). Another aspect of this study is that it uses water isotopic data sets of  $\delta^{18}\text{O}$  and  $\delta\text{D}$  measured using different analytical techniques, namely Isotope Ratio Mass Spectroscopy (**IRMS** hereafter) as well as Cavity Ring Down Spectroscopy (**CRDS** hereafter). Two of the data sets presented here were obtained using Continuous Flow Analysis (**CFA** hereafter) systems tailored for water isotopic analysis (Gkinis et al. 2011). All data sections are characterized by a very high sampling resolution typically of 5 cm or better.

## 2 THEORY

### 2.1 Diffusion of water isotope signals in firn

The porous medium of the top 60–80 m of firn allows for a molecular diffusion process that attenuates the water isotope signal from the time of deposition until pore close-off. The process takes place in the vapor phase and it can be described by Fick's second law as (assuming that the water isotope ratio signal ( $\delta$ ) approximates the concentration):

$$\frac{\partial \delta}{\partial t} = D(t) \frac{\partial^2 \delta}{\partial z^2} - \dot{\epsilon}_z(t) z \frac{\partial \delta}{\partial z} \quad (2.1)$$

where  $D(t)$  is the diffusivity coefficient,  $\dot{\epsilon}_z(t)$  the vertical strain rate and  $z$  is the vertical axis of a coordinate system, with its origin being fixed within the considered layer. The attenuation of the isotopic signal results in loss of information. However the dependence of  $\dot{\epsilon}_z(t)$  and  $D(t)$  on temperature and accumulation presents the possibility of using the process as a tool to infer these two paleoclimatic parameters. A solution to Eq. 2.1 can be given by the convolution of the initial isotopic profile  $\delta'$  with a Gaussian filter  $\mathcal{G}$  as:

$$\delta(z) = \mathcal{S}(z) [\delta'(z) * \mathcal{G}(z)] \quad (2.2)$$

where the Gaussian filter is described as:

$$\mathcal{G}(z) = \frac{1}{\sigma\sqrt{2\pi}} e^{-\frac{z^2}{2\sigma^2}}, \quad (2.3)$$

and  $\mathcal{S}$  is the total thinning of the layer at depth  $z$  described by

$$\mathcal{S}(z) = e^{\int_0^z \dot{\epsilon}_z(z') dz'}. \quad (2.4)$$

In Eq. 2.3, the standard deviation term  $\sigma^2$  represents the average displacement of a water molecule along the  $z$ -axis and is commonly referred to as the diffusion length. The  $\sigma^2$  quantity is a direct measure of diffusion and its accurate estimate is critical to any attempt of reconstructing temperatures that are based on the isotope diffusion thermometer. The diffusion length is directly related to the diffusivity coefficient and the strain rate (as the strain rate is approximately proportional to the densification rate in the firn column) and it can therefore be regarded as a measure of firn temperature.

The differential equation describing the evolution of  $\sigma^2$  with time is given by (Johnsen 1977):

$$\frac{d\sigma^2}{dt} - 2\dot{\epsilon}_z(t)\sigma^2 = 2D(t). \quad (2.5)$$

In the case of firn the following approximation can be made for the strain rate:

$$\dot{\epsilon}_z(t) \approx -\frac{d\rho}{dt} \frac{1}{\rho}, \quad (2.6)$$

with  $\rho$  representing the density. Then for the firn column, Eq. 2.5 can be solved hereby yielding a solution for  $\sigma^2$ :

$$\sigma^2(\rho) = \frac{1}{\rho^2} \int_{\rho_o}^{\rho} 2\rho^2 \left( \frac{d\rho}{dt} \right)^{-1} D(\rho) d\rho, \quad (2.7)$$

where  $\rho_o$  is the surface density. Under the assumption that the diffusivity coefficient  $D(\rho)$  and the densification rate  $\frac{d\rho}{dt}$  are known, integration from surface density  $\rho_o$  to the close-off density  $\rho_{co}$  can be performed yielding a model based estimate for the diffusion length. In this work we make use of the Herron–Langway densification model (**H–L hereafter**) and the diffusivity rate parametrization introduced by Johnsen et al. (2000) (see Appendix A).  $\frac{d\rho}{dt}$  depends on temperature and overburden pressure and  $D(\rho)$  depends on temperature and firn connectivity. Our implementation of Eq. 2.7 includes a seasonal temperature signal that propagates down in the firn is included (see Appendix B). The seasonal temperature variation affects the firn diffusion length nonlinearly in the upper 10 – 12 m due to the saturation vapor pressure’s exponential dependence on temperature.

In Fig. 2.1 we evaluate Eq. 2.7 for all three isotopic ratios of water ( $\delta^{18}\text{O}$ ,  $\delta^{17}\text{O}$ ,  $\delta\text{D}$ ) using boundary conditions characteristic of ice core sites from central Greenland and the East Antarctic Ice Cap. In Fig. 2.1, the transition between zone 1 and zone 2 densification (at the critical density  $\rho_c = 550 \text{ kgm}^{-3}$ ) is evident as a kink in both the densification and diffusion model. For the first case we consider cold and dry conditions (case **A** hereafter) representative of Antarctic ice coring sites (e.g. Dome C, Vostok) with a surface temperature  $T_{\text{sur}} = -55^\circ\text{C}$  and annual accumulation  $A = 0.032 \text{ myr}^{-1} \text{ ice eq.}$  For the second case we consider relatively warm and humid conditions (case **B** hereafter) representative of central Greenlandic ice coring sites (e.g. GISP2, GRIP, NorthGRIP) with a surface temperature  $T_{\text{sur}} = -29^\circ\text{C}$  and annual accumulation  $A = 0.22 \text{ myr}^{-1} \text{ ice eq.}$  The general impact of surface temperature and accumulation rate on the firn diffusion length can be seen in Fig. 2.2.

## 2.2 Isotope diffusion in the solid phase

Below the close-off depth, diffusion occurs in solid ice driven by the isotopic gradients within the lattice of the ice crystals. This process is several orders of magnitude slower than firn diffusion. Several studies exist that deal with the estimate of the diffusivity coefficient in ice (Itagaki 1964, Blinks et al. 1966, Delibaltas et al. 1966, Ramseier 1967, Livingston et al. 1997). The differences resulting from the various diffusivity coefficients are small and negligible for the case of our study (for a brief comparison between the different parameterizations, the reader is referred to Gkinis et al. (2014)). As done before

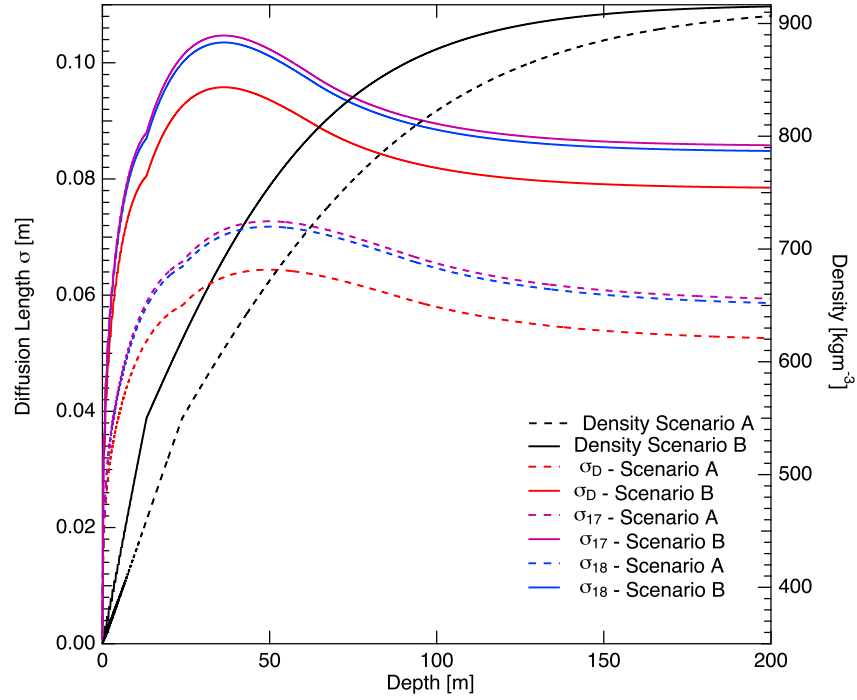


Figure 2.1: Diffusion length and density profiles (black) for case A (dashed lines:  $T_{\text{sur}} = -55^\circ\text{C}$ ,  $A = 0.032 \text{ myr}^{-1}$ ) and B (solid curves:  $T_{\text{sur}} = -29^\circ\text{C}$ ,  $A = 0.22 \text{ myr}^{-1}$ ). The increase in diffusion of the  $\delta^{18}\text{O}$  (blue color),  $\delta^{17}\text{O}$  (purple color) and  $\delta\text{D}$  (red color) isotope signals are partially due to the compaction of the firn which moves the ice closer together.

141 by other similar firn diffusion studies (Johnsen et al. 2000, Simonsen et al. 2011, Gkinis et al. 2014) we  
 142 make use of the parametrization given in Ramseier (1967) as:

$$D_{\text{ice}} = 9.2 \cdot 10^{-4} \cdot \exp\left(-\frac{7186}{T}\right) \text{ m}^2\text{s}^{-1}. \quad (2.8)$$

143 Assuming that a depth–age scale as well as a thinning function are available for the ice core a solution  
 144 for the ice diffusion length is given by (see Appendix C for details):

$$\sigma_{\text{ice}}^2(t') = S(t')^2 \int_0^{t'} 2D_{\text{ice}}(t) S(t)^{-2} dt. \quad (2.9)$$

145 In Fig. 2.3 we have calculated ice diffusion lengths for four different cores (NGRIP, NEEM, Dome C,  
 146 EDML). For the calculation of  $D_{\text{ice}}$  we have used the borehole temperature profile of each core and  
 147 assumed a steady state condition. As the temperature of the ice increases closer to the bedrock,  $\sigma_{\text{ice}}$   
 148 increases nonlinearly due to  $D_{\text{ice}}$  exponential temperature dependence. When approaching these deeper  
 149 parts of the core, the warmer ice temperatures enhance the effect of ice diffusion which then becomes

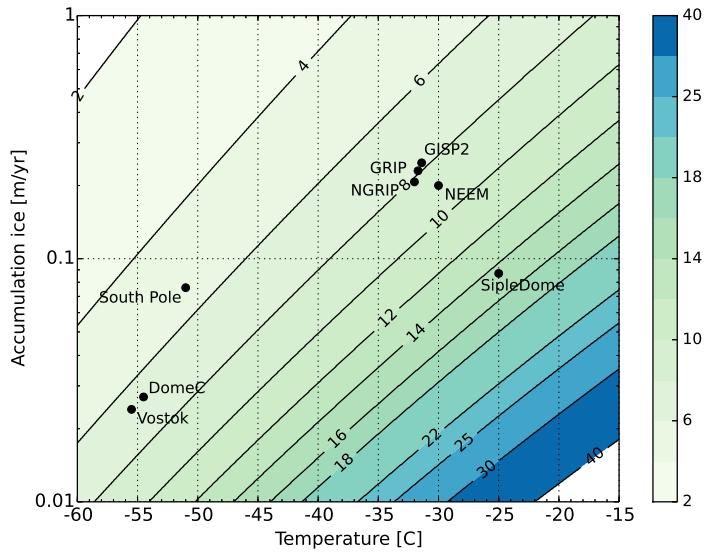


Figure 2.2: Modeled firn diffusion lengths [cm] for  $\delta^{18}\text{O}$  as a function of temperature and accumulation rate (with  $\rho_{\text{co}} = 804\text{kgm}^{-3}$  and  $\rho_o = 330\text{kgm}^{-3}$ ) from Gkinis et al. (2014). The contours indicate lines of constant diffusion length and the colorbar represents the diffusion length in cm. Here the combined impact of temperature and accumulation rate on the diffusion length is evident; while warm temperatures induce high diffusion lengths, a high accumulation rate reduces the diffusion length estimate. The firn diffusion lengths corresponding to a few ice core sites are plotted as a reference.

an important and progressively dominating factor in the calculations. For the special case of the Dome C core (with a bottom age exceeding 800,000 years),  $\sigma_{\text{ice}}$  reaches values as high as 15 cm.

### 3 RECONSTRUCTING FIRN TEMPERATURES FROM ICE CORE DATA

Here we outline the various temperature reconstruction techniques that can be employed for paleotemperature reconstructions. In order to avoid significant overlap with previously published works e.g. Johnsen (1977), Johnsen et al. (2000), Simonsen et al. (2011), Gkinis et al. (2014), van der Wel et al. (2015) we occasionally point the reader to any of the latter or/and refer to specific sections in the Appendix. We exemplify and illustrate the use of various techniques using synthetic data prepared such that they resemble two representative regimes of ice coring sites on the Greenland summit and the East Antarctic Plateau.

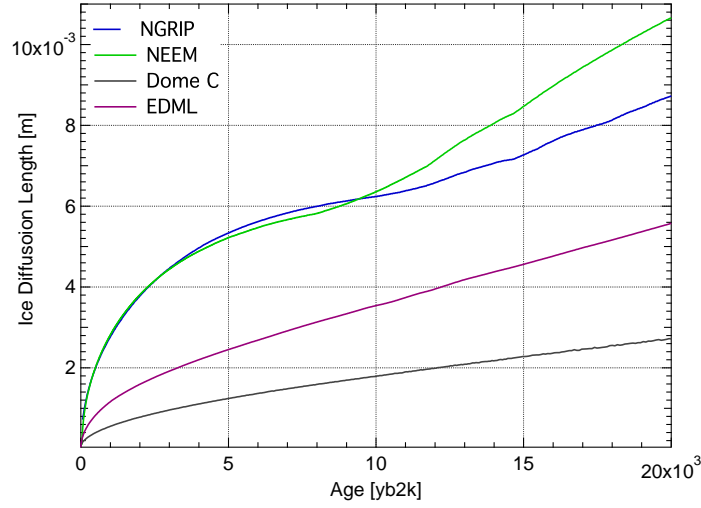


Figure 2.3: The ice diffusion length plotted with respect to age [b2k] for some selected sites from Greenland (NGRIP and NEEM) and Antarctica (Dome C and EDML).

### 3.1 The single isotopologue diffusion

As shown in Eq. 2.2, the impact of the diffusion process can be mathematically described as a convolution of the initial isotopic profile with a Gaussian filter. A fundamental property of the convolution operation is that it is equivalent to multiplication in the frequency domain. The transfer function for the diffusion process will be given by the Fourier transform of the Gaussian filter that will itself be a Gaussian function described by (Abramowitz & Stegun 1964, Gkinis et al. 2014):

$$\mathfrak{F}[\mathcal{G}(z)] = \hat{\mathcal{G}} = e^{\frac{-k^2 \sigma^2}{2}}. \quad (3.1)$$

In Eq. 3.1,  $k = 2\pi f$  where  $f$  is the frequency of the isotopic time series. In Fig. 3.1 we illustrate the effect of the diffusion transfer function on a range of wavelengths for  $\sigma = 1, 2, 4$  and  $8$  cm. Frequencies corresponding to wavelengths on the order of  $50$  cm and above remain largely unaltered while signals with wavelengths shorter than  $20$  cm are heavily attenuated.

A data-based estimate of the diffusion length  $\sigma$  can be obtained by looking at the power spectrum of the diffused isotopic time series. Assuming a noise signal  $\eta(k)$ , Eq. 3.1 provides a model describing the power spectrum as:

$$P_s = P_0(k)e^{-k^2 \sigma^2} + |\hat{\eta}(k)|^2, \quad f \in [0, f_{Nq}] \quad (3.2)$$

where  $f_{Nq} = 1/(2\Delta)$  is the Nyquist frequency that is defined by the sampling resolution  $\Delta$ .  $P_0(k)$  is the spectral density of the compressed profile without diffusion. It is assumed independent of  $k$  (now



$P_0$ ) due to the strong depositional noise encountered in high resolution  $\delta$  ice core series (Johnsen et al. 2000). Theoretically  $|\hat{\eta}(k)|^2$  refers to white measurement noise. As we will show later, real ice core data sometimes have a more red noise behavior. A generalized model for the noise signal can be described well by autoregressive process of order 1 (AR-1). Its power spectral density is defined as (Kay & Marple 1981):

$$|\hat{\eta}(k)|^2 = \frac{\sigma_\eta^2 \Delta}{|1 - a_1 \exp(-ik\Delta)|^2}, \quad (3.3)$$

where  $a_1$  is the AR-1 coefficient and  $\sigma_\eta^2$  is the variance of the noise signal.

In Fig. 3.2, an example of power spectra based on a synthetic time series is shown. A description of how the synthetic time series is generated is provided in Appendix D. The diffusion length used for the power spectrum in Fig. 3.2 is equal to 8.50 cm. The spectral estimate of the time series  $\mathbb{P}_s$  is calculated using Burg's spectral estimation method (Kay & Marple 1981) and specifically the algorithm presented in Andersen (1974). Using a least-squares approach we optimize the fit of the model  $P_s$  to the data-based  $\mathbb{P}_s$  by varying the four parameters  $P_0$ ,  $\sigma$ ,  $a_1$  and  $\sigma_\eta^2$ . In the case of Fig. 3.2, the  $|P_s - \mathbb{P}_s|^2$  least squares optimization resulted in  $P_0 = 0.35 \text{ } \text{‰}^2 \cdot \text{m}$ ,  $\sigma = 8.45 \text{ cm}$ ,  $a_1 = 0.05$  and  $\sigma_\eta^2 = 0.005 \text{ } \text{‰}^2$ .

Assuming a diffusion length  $\hat{\sigma}_i^2$  is obtained for depth  $z_i$  by means of  $|P_s - \mathbb{P}_s|^2$  minimization, one can calculate the equivalent diffusion length at the bottom of the firn column  $\sigma_{\text{firn}}^2$  in order to estimate firn temperatures by means of Eq. 2.7. In order to do this, one needs to take into account three necessary corrections - (1) sampling diffusion, (2) ice diffusion and (3) thinning. The first concerns the artifactually imposed diffusion due to the sampling of the ice core. In the case of a discrete sampling scheme with resolution  $\Delta$  the additional diffusion length is (see Appendix E):

$$\sigma_{\text{dis}}^2 = \frac{2\Delta^2}{\pi^2} \ln\left(\frac{\pi}{2}\right). \quad (3.4)$$

In the case of high resolution measurements carried out with CFA measurement systems, there exist a number of ways to characterize the sampling diffusion length. Typically the step or impulse response of the CFA system can be measured yielding a Gaussian filter specific for the CFA system (Gkinis et al. 2011, Maselli et al. 2013, Emanuelsson et al. 2015, Jones et al. 2017). The Gaussian filter can be characterized by a diffusion length  $\sigma_{\text{cfa}}^2$  that can be directly used to perform a sampling correction. The second correction concerns the ice diffusion as described in Sec. 2.2. The quantities  $\sigma_{\text{ice}}^2$  and  $\sigma_{\text{dis}}^2$  can be subtracted from  $\hat{\sigma}_i^2$  yielding a scaled value of  $\sigma_{\text{firn}}^2$  due to ice flow thinning. As a result, we can finally obtain the diffusion length estimate at the bottom of the firn column  $\sigma_{\text{firn}}^2$  (in meters of ice eq.):

$$\sigma_{\text{firn}}^2 = \frac{\hat{\sigma}_i^2 - \sigma_{\text{dis}}^2 - \sigma_{\text{ice}}^2}{S(z)^2}. \quad (3.5)$$

Subsequently, a temperature estimate can be obtained by numerically finding the root of (for a known  $A(z)$ ):

$$\left(\frac{\rho_{co}}{\rho_i}\right)^2 \sigma^2(\rho = \rho_{co}, T(z), A(z)) - \sigma_{firn}^2 = 0 \quad (3.6)$$

where  $\sigma^2$  is the result of the integration in Eq. 2.7 from surface to close-off density ( $\rho_o \rightarrow \rho_{co}$ ). In this work we use a Newton-Raphson numerical scheme (Press et al. 2007) for the calculation of the root of the equation.

The accuracy of the  $\sigma_{firn}^2$  estimation and subsequently of the temperature reconstruction obtained based on it, depends on the three correction terms  $\sigma_{ice}^2$ ,  $\sigma_{dis}^2$  and the ice flow thinning  $\mathcal{S}(z)$ . For relatively shallow depths where  $\sigma_{ice}^2$  is relatively small compared to  $\hat{\sigma}_i^2$ , ice diffusion can be accounted for with simple assumptions on the borehole temperature profile and the ice flow. In a similar way,  $\sigma_{dis}^2$  is a well constrained parameter and depends only on the sampling resolution  $\Delta$  for discrete sampling schemes or the smoothing of the CFA measurement system.

Equation 3.5 reveals an interesting property of the single isotopologue temperature estimation technique. As seen, the result of the  $\sigma_{firn}^2$  calculation depends strongly on the ice flow thinning quantity  $\mathcal{S}(z)^2$ . Possible errors in the estimation of  $\mathcal{S}(z)^2$  due to imperfections in the modelling of the ice flow will inevitably be propagated to the  $\sigma_{firn}^2$  value thus biasing the temperature estimation. Even though this appears to be a disadvantage of the method, in some instances, it can be a useful tool for assessing the accuracy of ice flow models. Provided that for certain sections of the ice core there is a temperature estimate available based on other reconstruction methods (borehole thermometry,  $\delta^{15}\text{N}$ /  $\delta^{40}\text{Ar}$ ) it is possible to estimate ice flow induced thinning of the ice core layers. Following this approach Gkinis et al. (2014) proposed a correction in the existing accumulation rate history for the NorthGRIP ice core.

### *The annual spectral signal interference*

Depending on the ice core site temperature and accumulation conditions, spectral signatures of an annual isotopic signal can be apparent as a peak located at the frequency range that corresponds to the annual layer thickness. The resulting effect of such a spectral signature, is the artifactual biasing of the diffusion length estimation towards lower values and thus colder temperatures. Figure 3.3 shows the PSD of the  $\delta\text{D}$  series for a mid Holocene section from the GRIP ice core (drill site characteristics in Table 4.3). A prominent spectral feature is visible at  $f \approx 6 \text{ cycles m}^{-1}$ . This frequency is comparable to the expected frequency of the annual signal at  $6.1 \text{ cycles m}^{-1}$  as estimated from the annual layer thickness reconstruction of the GICC05 timescale (Vinther et al. 2006).

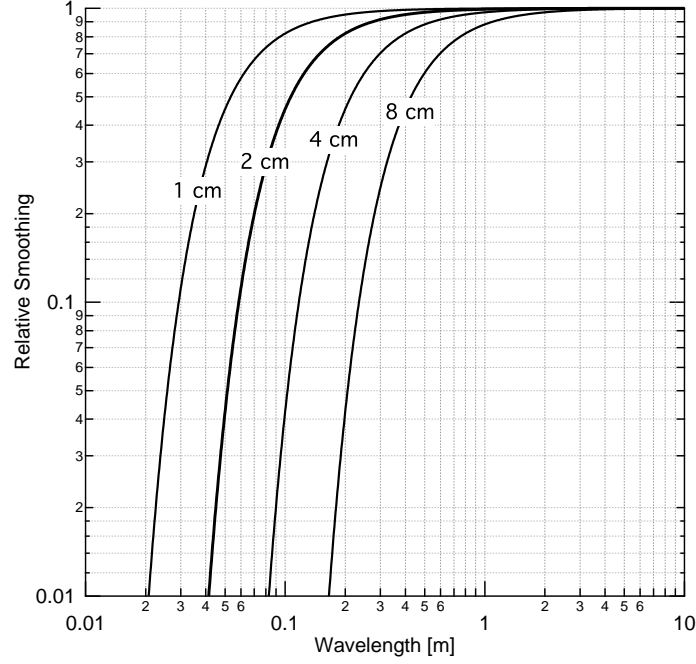


Figure 3.1: The smoothing effect of the diffusion transfer function demonstrated on a range of different wavelengths for  $\sigma = 1, 2, 4$  and  $8$  cm.

In order to evade the influence of the annual spectral signal on the diffusion length estimation, we propose the use of a weight function  $w(f)$  in the spectrum as:

$$w(f) = \begin{cases} 0 & f_{\lambda} - df_{\lambda} \leq f \leq f_{\lambda} + df_{\lambda} \\ 1 & f < f_{\lambda} - df_{\lambda}, f > f_{\lambda} + df_{\lambda} \end{cases} \quad (3.7)$$

where  $f_{\lambda}$  is the frequency of the annual layer signal based on the reconstructed annual layer thickness  $\lambda$  and  $df_{\lambda}$  is the range around the frequency  $f_{\lambda}$  at which the annual signal is detectable. The weight function is multiplied with the optimization norm  $|P_s - \mathbb{P}_s|^2$ . Figure 3.3 also illustrates the effect of the weight function on the estimation of  $P_s$  and subsequently the diffusion length value. When the weight function is used during the optimization process, there is an increase in the diffusion length value by  $0.3$  cm, owing essentially to the exclusion of the annual signal peak from the minimization of  $|P_s - \mathbb{P}_s|^2$ . While the value of  $f_{\lambda}$  can be roughly predicted, the value of  $df_{\lambda}$  usually requires visual inspection of the spectrum. We used a weight function of  $w(f_{\lambda} - 0.5 \leq f \leq f_{\lambda} + 3) = 0$ .

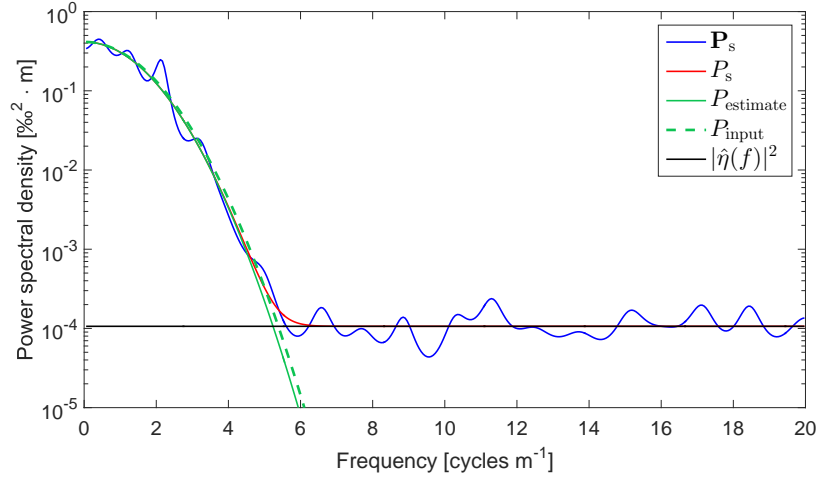


Figure 3.2: PSD of a synthetic  $\delta^{18}\text{O}$  time series plotted with respect to frequency (blue curve). The red curve represents the complete model fit (Eq. 3.2). The green dashed curve represents the input diffusion and the solid green curve represents the estimated diffusion length of the signal (uncorrected for sampling diffusion). The black curve represents the noise part of the fit.

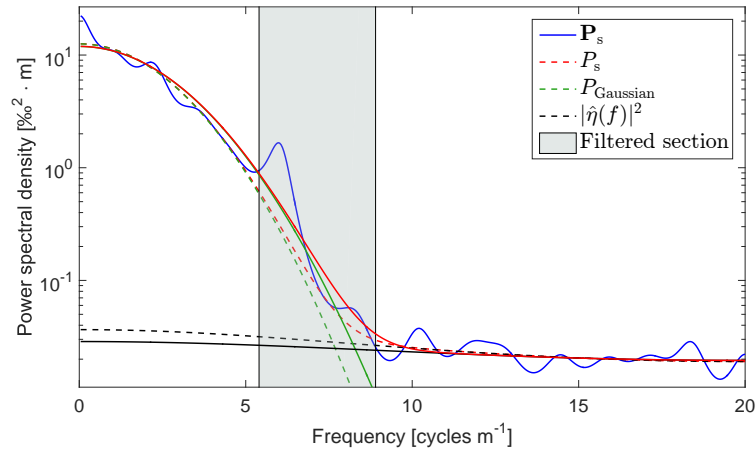


Figure 3.3: The interference of the annual spectral signal is seen in the PSD of the  $\delta\text{D}$  GRIP mid Holocene section. The regular fit is represented by the solid lines and the dashed lines represent the case where the weight function  $w(f)$  has filtered out this artifactual bias.

### 3.2 The differential diffusion signal

A second-order temperature reconstruction technique is possible based on the differential signal between  $\delta^{18}\text{O}$  and  $\delta\text{D}$ . Due to the difference in the fractionation factors and the air diffusivities between the oxygen and deuterium isotopologues, a differential diffusion signal is created in the firn column. Based on the calculation of the diffusion lengths presented in Fig. 2.1 we then compute the differential diffusion lengths  $^{17}\Delta\sigma^2$  and  $^{18}\Delta\sigma^2$  where

$$^{17}\Delta\sigma^2 = \sigma_{17}^2 - \sigma_{\text{D}}^2 \text{ and } ^{18}\Delta\sigma^2 = \sigma_{18}^2 - \sigma_{\text{D}}^2. \quad (3.8)$$

As it can be seen in Fig. 3.4 the differential diffusion length signal is slightly larger for the case of  $^{17}\Delta\sigma^2$  when compared to  $^{18}\Delta\sigma^2$ .

One obvious complication of the differential diffusion technique is the requirement for dual measurements of the water isotopologues, preferably performed on the same sample. The evolution of IRMS techniques targeting the analysis of  $\delta\text{D}$  (Bigeleisen et al. 1952, Vaughn et al. 1998, Gehre et al. 1996, Begley & Scrimgeour 1997) in ice cores has allowed for dual isotopic records at high resolutions. With the advent of CRDS techniques and their customization for CFA measurements, simultaneous high resolution measurements of both  $\delta^{18}\text{O}$  and  $\delta\text{D}$  have become a routine procedure.

The case of  $\delta^{17}\text{O}$  is more complicated as the greater abundance of  $^{13}\text{C}$  than  $^{17}\text{O}$  rules out the possibility for an IRMS measurement at mass/charge ratio ( $m/z$ ) of 45 or 29 using  $\text{CO}_2$  equilibration or reduction to  $\text{CO}$  respectively. Alternative approaches that exist include the electrolysis method with  $\text{CuSO}_4$  developed by Meijer & Li (1998) as well as the fluorination method presented by Baker et al. (2002) and implemented by Barkan & Luz (2005) for dual-inlet IRMS systems. These techniques target the measurement of the  $^{17}\text{O}_{\text{excess}}$  parameter and are inferior for  $\delta^{17}\text{O}$  measurements at high precision and have a very low sample throughput. As a result, high resolution  $\delta^{17}\text{O}$  measurements from ice cores are currently non existent. Recent innovations however in CRDS spectroscopy (Steig et al. 2014) allow for simultaneous triple isotopic measurements of  $\delta\text{D}$ ,  $\delta^{18}\text{O}$  and  $\delta^{17}\text{O}$  in a way that a precise and accurate measurement for both  $\delta^{17}\text{O}$  and  $^{17}\text{O}_{\text{excess}}$  is possible. Therefore high resolution ice core datasets of  $\delta\text{D}$ ,  $\delta^{18}\text{O}$  and  $\delta^{17}\text{O}$  should be expected in the near future.

The following analysis is focused on the  $^{18}\Delta\sigma^2$  signal but it applies equally to the  $^{17}\Delta\sigma^2$ . The stronger attenuation of the  $\delta^{18}\text{O}$  signal with respect to the  $\delta\text{D}$  signal can be visually observed in the power spectral densities of the two signals. As seen in Fig. 3.5 the  $\mathbb{P}_{\text{S18}}$  signal reaches the noise level at a lower frequency when compared to the  $\mathbb{P}_{\text{SD}}$  signal. At low frequencies with high signal to noise ratio we can calculate the logarithm of the ratio of the two power spectral densities as (i.e. neglecting the noise term):

$$\ln\left(\frac{P_{\text{D}}}{P_{18}}\right) \approx k^2 (\sigma_{18}^2 - \sigma_{\text{D}}^2) + \ln\left(\frac{P_{0\text{D}}}{P_{018}}\right) = ^{18}\Delta\sigma^2 k^2 + C. \quad (3.9)$$

As seen in Eq. 3.9 and Fig. 3.5 (synthetic generated  $\delta^{18}\text{O}$  and  $\delta\text{D}$  data as in Sec. 3.1) an estimate of the  $^{18}\Delta\sigma^2$  parameter can be obtained by a linear fit of  $\ln(P_{\text{D}}/P_{18})$  in the low frequency area, thus requiring only two parameters ( $^{18}\Delta\sigma^2$  and  $C$ ) to be tuned. An interesting aspect of the differential diffusion method, is that in contrast to the single isotopologue diffusion length,  $^{18}\Delta\sigma_{\text{firn}}^2$  is a quantity that is independent of the sampling and solid ice diffusion thus eliminating the uncertainties associated with these two parameters. This can be seen by simply using Eq. 3.5:

$$^{18}\Delta\sigma_{\text{firn}}^2 = \frac{\hat{\sigma}_{18}^2 - \sigma_{\text{dis}}^2 - \sigma_{\text{ice}}^2}{S(z)^2} - \frac{\hat{\sigma}_{\text{D}}^2 - \sigma_{\text{dis}}^2 - \sigma_{\text{ice}}^2}{S(z)^2} = \frac{\hat{\sigma}_{18}^2 - \hat{\sigma}_{\text{D}}^2}{S(z)^2}. \quad (3.10)$$

Accurate estimates of the thinning function however still play a key role in the differential diffusion technique. One more complication of the differential diffusion technique is the selection of the frequency range in which one chooses to apply the linear regression. Often visual inspection is required in order to designate a cut-off frequency until which the linear regression can be applied. In most cases identifying the cut-off frequency, or at least a reasonable area around it is reasonably straight-forward. Though in a small number of cases, spectral features in the low frequency area seem to have a strong influence on the slope of the linear regression and thus on the  $^{18}\Delta\sigma^2$ . As a result, visual inspection of the regression result is always advised in order to avoid biases.

Another way of estimating the differential diffusion signal is to subtract the single diffusion spectral estimates  $\sigma_{18}^2$  and  $\sigma_{\text{D}}^2$ . Theoretically this approach should be inferior to the linear fit approach due to the fact that more degrees of freedom are involved in the estimation of  $\sigma_{18}^2$  and  $\sigma_{\text{D}}^2$  (8 versus 2; 3 if the cutoff frequency is included). Here we will test both approaches.

### *Linear correlation method*

An alternative way to calculate the differential diffusion signal  $^{18}\Delta\sigma^2$  is based on the assumption that the initial precipitated isotopic signal presents a deuterium excess signal  $d_{\text{xs}}$  that is invariable with time and as a consequence of this, the correlation signal between  $\delta^{18}\text{O}$  and  $\delta\text{D}$  (hereafter  $r_{\delta^{18}\text{O}/\delta\text{D}}$ ) is expected to have a maximum value at the time of deposition. The  $d_{\text{xs}}$  signal is defined as the deviation from the meteoric water line  $d_{\text{xs}} = \delta\text{D} - 8 \cdot \delta^{18}\text{O}$  (Craig 1961, Dansgaard 1964). From the moment of deposition, the difference in diffusion between the  $\delta^{18}\text{O}$  and  $\delta\text{D}$  signals results in a decrease of the  $r_{\delta^{18}\text{O}/\delta\text{D}}$  value. Hence, diffusing the  $\delta\text{D}$  signal with a Gaussian kernel of standard deviation equal to  $^{18}\Delta\sigma^2$  will maximize the value of  $r_{\delta^{18}\text{O}/\delta\text{D}}$  (van der Wel et al. 2015) as shown in Fig. 3.6. Thus, the  $^{18}\Delta\sigma^2$  value is found when the  $r_{\delta^{18}\text{O}/\delta\text{D}}$  value has its maximum.

This type of estimation is independent of spectral estimates of the  $\delta^{18}\text{O}$  and  $\delta\text{D}$  time series and does not pose any requirements for measurement noise characterization or selection of cut-off frequencies.

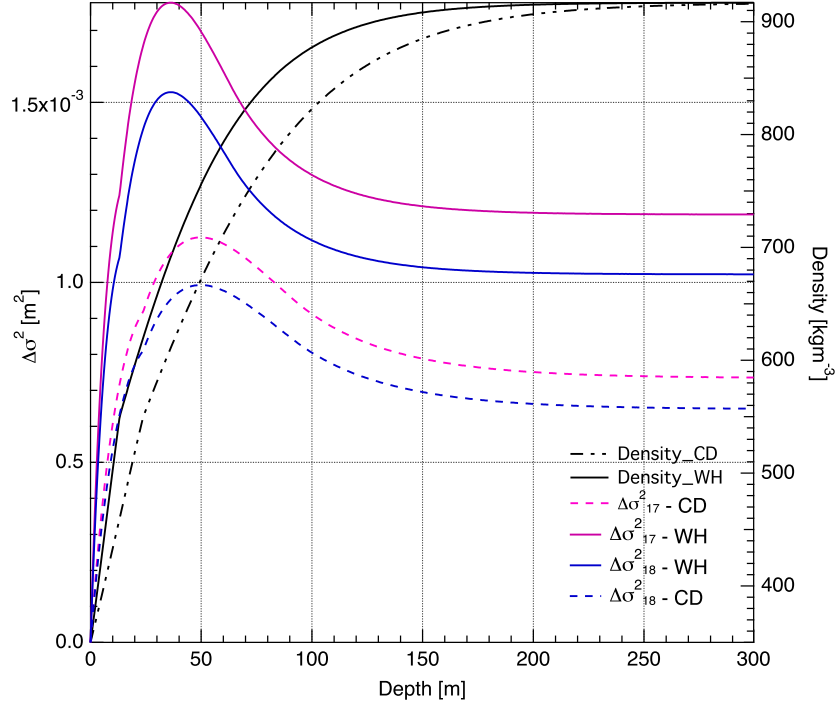


Figure 3.4: Differential diffusion length profiles for cases A (dashed lines) and B (solid lines) for  $^{18}\Delta\sigma^2$  (blue) and  $^{17}\Delta\sigma^2$  (purple). The density profiles are given in black.

However uncertainties related to the densification and ice flow processes, affect this method equally as they do for the spectrally based differential diffusion temperature estimation. In this study, we test the applicability of the method on synthetic and real ice core data. We acknowledge that the assumption that the  $d_{xs}$  signal is constant with time is not entirely consistent with the fact that there is a small seasonal cycle in the  $d_{xs}$  signal (Johnsen & White 1989). It is thus likely to result in inaccuracies.

### 3.3 The diffusion length ratio

A third way of using the diffusion lengths as proxies for temperature can be based on the calculation of the ratio of two different diffusion lengths. From Eq. 2.7 we can evaluate the ratio of two different isotopologues  $j$  and  $k$  as:

$$\frac{\sigma_j^2(\rho)}{\sigma_k^2(\rho)} = \frac{\frac{1}{\rho^2} \int 2\rho^2 \left(\frac{d\rho}{dt}\right)^{-1} D_j(\rho) d\rho}{\frac{1}{\rho^2} \int 2\rho^2 \left(\frac{d\rho}{dt}\right)^{-1} D_k(\rho) d\rho}, \quad (3.11)$$

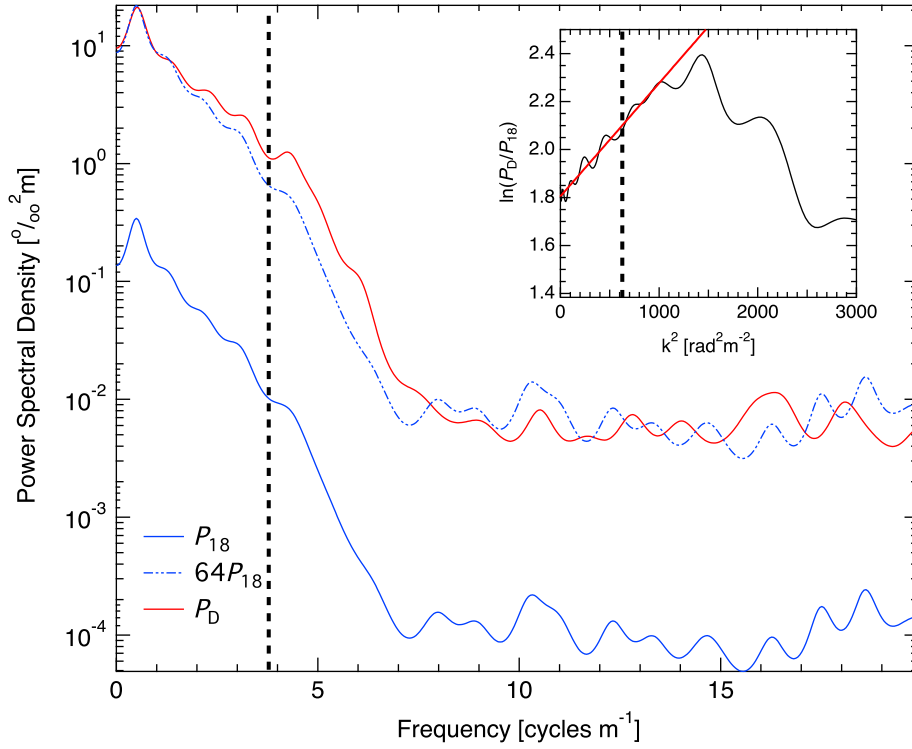


Figure 3.5: PSDs of synthetic  $\delta^{18}\text{O}$  (blue) and  $\delta\text{D}$  (red) with respect to frequency where the inner subplot shows the  $\ln(P_D/P_{18})$  relation with respect to  $k^2$ . The  $^{18}\Delta\sigma^2$  value is determined from the slope of the linear fit in the subplot. The chosen cutoff frequency is marked by the vertical dashed line in both plots.

311 and by substituting the firm diffusivities as defined in Appendix A and according to Johnsen et al. (2000)  
 312 we get:

$$\frac{\sigma_j^2(\rho)}{\sigma_k^2(\rho)} = \frac{D_{aj}\alpha_k}{D_{ak}\alpha_j} \frac{\frac{1}{\rho^2} \int 2\rho^2 \left(\frac{d\rho}{dt}\right)^{-1} \frac{mp}{RT\tau} \left(\frac{1}{\rho} - \frac{1}{\rho_{\text{ice}}}\right) d\rho}{\frac{1}{\rho^2} \int 2\rho^2 \left(\frac{d\rho}{dt}\right)^{-1} \frac{mp}{RT\tau} \left(\frac{1}{\rho} - \frac{1}{\rho_{\text{ice}}}\right) d\rho} = \frac{D_{aj}\alpha_k}{D_{ak}\alpha_j}. \quad (3.12)$$

313 As a result, the ratio of the diffusion lengths is dependent on temperature through the parameterizations  
 314 of the fractionation factors ( $\alpha$ ) and carries no dependence to parameters related to the densification rates  
 315 nor the atmospheric pressure. Additionally, it is a quantity that is independent of depth. Here we give  
 316 the analytical expressions of all the isotopologues combinations by substituting the diffusivities and the



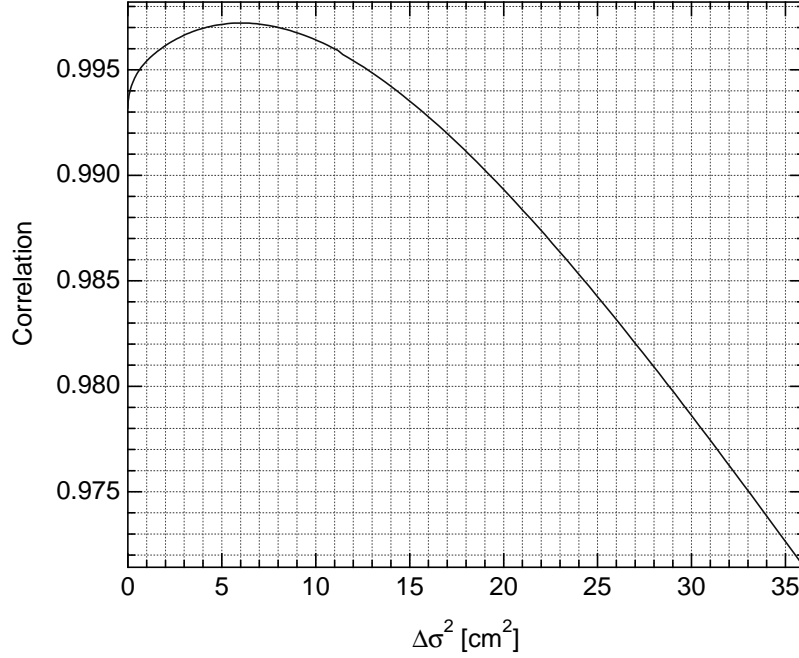


Figure 3.6: Correlation coefficient ( $r_{\delta^{18}\text{O}/\delta\text{D}}$ ) between the  $\delta^{18}\text{O}$  and the forward-diffused  $\delta\text{D}$  series as a function of the estimated  $^{18}\Delta\sigma^2$ . The synthetic data represent a case A climate.

fractionation factors:

$$\sigma_{18}^2/\sigma_{\text{D}}^2 = 0.93274 \cdot \exp(16288/T^2 - 11.839/T) \quad (3.13)$$

$$\sigma_{17}^2/\sigma_{\text{D}}^2 = 0.933 \cdot \exp(16288/T^2 - 6.263/T) \quad (3.14)$$

$$\sigma_{18}^2/\sigma_{17}^2 = 0.99974 \cdot \exp(-5.57617/T) \quad (3.15)$$

A data-based diffusion length ratio estimate can be obtained by estimating the single diffusion length values as described in Sec. 3.1 and thereafter applying the necessary corrections as in Eq. 3.5. An interesting aspect of the ratio estimation is that it is not dependent on the ice flow thinning as seen below

$$\left(\frac{\sigma_{18}^2}{\sigma_{\text{D}}^2}\right)_{\text{firn}} = \frac{\hat{\sigma}_{18}^2 - \sigma_{\text{dis}}^2 - \sigma_{\text{ice}}^2}{\hat{\sigma}_{\text{D}}^2 - \sigma_{\text{dis}}^2 - \sigma_{\text{ice}}^2}. \quad (3.16)$$

while the method still depends on the sampling and ice diffusion.

## 4 RESULTS

### 4.1 Synthetic data test

A first order test for the achievable accuracy and precision of the presented diffusion temperature reconstruction techniques can be performed using synthetic isotopic data. We generate synthetic time

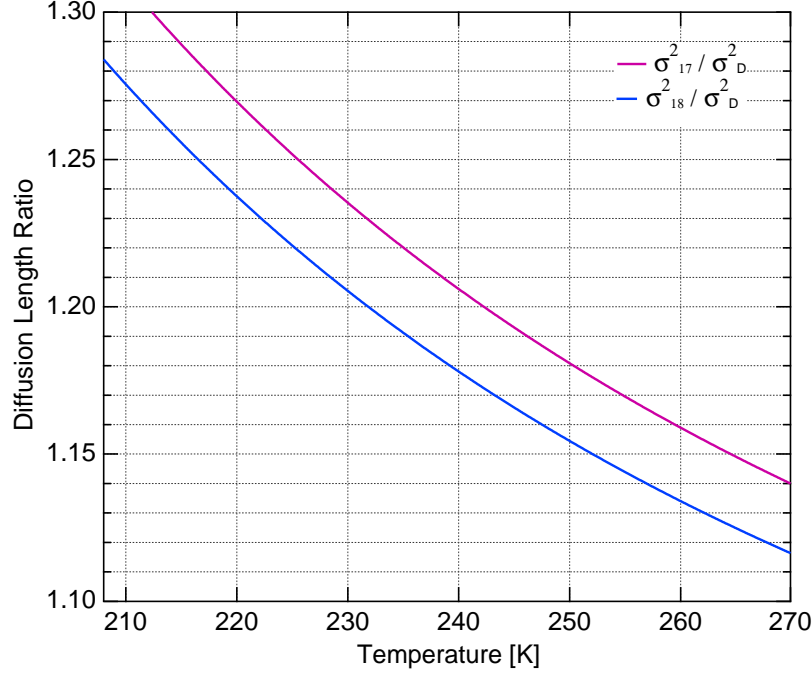


Figure 3.7: The diffusion length ratios  $\sigma_{18}^2/\sigma_D^2$  and  $\sigma_{17}^2/\sigma_D^2$  with respect to temperature. The  $\sigma_{18}^2/\sigma_{17}^2$  is almost constant at 0.975 and omitted here due to its very low temperature sensitivity.

series of  $\delta^{17}\text{O}$ ,  $\delta^{18}\text{O}$  and  $\delta\text{D}$  using an AR-1 process and subsequently applying numerical diffusion with diffusion lengths as calculated for case A and B (as presented in Fig. 2.1). The time series are then sampled at a resolution of 2.5 cm and white measurement noise is added. Eventually, estimates of diffusion lengths for all three isotopologues are obtained using the techniques we have described in the previous sections. A more detailed description of how the synthetic data are generated is outlined in Appendix D.

The process of time series generation is repeated 500 times. For each iteration, the quantities  $\sigma_{17}$ ,  $\sigma_{18}$ ,  $\sigma_D$ ,  $^{17}\Delta\sigma^2$ ,  $^{18}\Delta\sigma^2$  and the ratios  $\sigma_{18}^2/\sigma_D^2$ ,  $\sigma_{17}^2/\sigma_D^2$  and  $\sigma_{18}^2/\sigma_{17}^2$  are estimated. The differential diffusion signals are estimated using the three different techniques as described in Sec. 3.2. We designate the subtraction technique with I, the linear regression with II and the correlation method with III. For every value of the diffusion estimates we calculate a firm temperature where the uncertainties related to the firm diffusion model ( $A$ ,  $\rho_{co}$ ,  $\rho_o$ , surface pressure  $P$ ,  $S$  and  $\sigma_{ice}$  in Table 4.1) are included. For the total of the 500 iterations we calculate a mean firm temperature  $\bar{T}$ , a standard deviation and a mean bias as:

$$\text{MB} = \frac{1}{N} \sum_{i=1}^N T_i - T_{\text{sur}} = \bar{T} - T_{\text{sur}}, \quad (4.1)$$

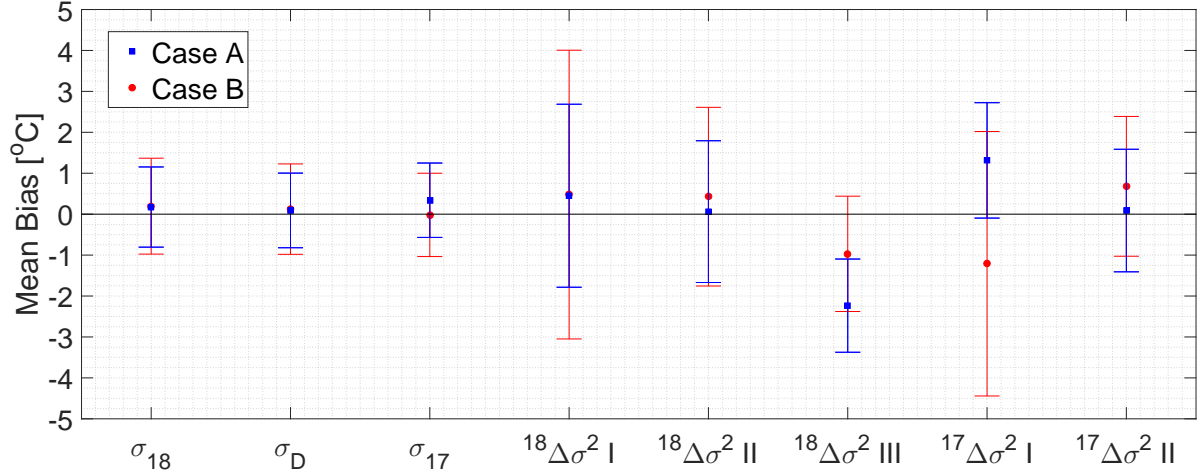


Figure 4.1: Mean biases for the single and differential diffusion techniques. The error bars represent 1 std of the estimated temperatures.

where  $i = 1, 2, \dots, N$  signifies the iteration number,  $T_i$  is the synthetic data-based estimated temperature and  $T_{\text{sur}}$  is the model forcing surface temperature for the case A and B scenarios. The results of the experiment are presented in Table 4.2 and the calculated mean biases are illustrated in Fig. 4.1. The diffusion length ratio approach yields very large uncertainty bars (see Table 4.2) and thus these results are not included in Fig. 4.1.

Table 4.1: The standard deviations of the input parameters. Most of the standard deviations are expressed as a percentage of the mean input value.

Parameter	$A$	$\rho_{co}$	$\rho_o$	$P$	$S$	$\sigma_{ice}$
Uncertainty	$\pm 5\% A_{\text{mean}}$	$\pm 20 \text{ kgm}^{-3}$	$\pm 30 \text{ kgm}^{-3}$	$\pm 2\% P_{\text{mean}}$	$\pm 1\% S_{\text{mean}}$	$\pm 2\% \sigma_{ice_{\text{mean}}}$

## 4.2 Ice core data test

We also use a number of high resolution, high precision ice core data, in order to benchmark the diffusion temperature reconstruction techniques that we have presented. The aim of this benchmark test is to utilize the various reconstruction techniques for a range of boundary conditions that is (a) as broad as possible with respect to mean annual surface temperature and accumulation and (b) representative of existing polar ice core sites. Additionally, we have made an effort in focusing on ice core data sets that

	Case A			Case B		
	Applied diffusion	Est. diffusion	Est. T [°C]	Applied diffusion	Est. diffusion	Est. T [°C]
$\sigma_{18}$	5.82 cm	$5.85 \pm 0.14$ cm	$-54.8 \pm 1.0$	8.50 cm	$8.51 \pm 0.20$ cm	$-28.8 \pm 1.2$
$\sigma_D$	5.22 cm	$5.23 \pm 0.12$ cm	$-54.9 \pm 0.9$	7.86 cm	$7.86 \pm 0.18$ cm	$-28.9 \pm 1.1$
$\sigma_{17}$	5.90 cm	$5.97 \pm 0.11$ cm	$-54.7 \pm 0.9$	8.59 cm	$8.54 \pm 0.13$ cm	$-29.0 \pm 1.0$
$^{18}\Delta\sigma^2$ I	6.6 cm <sup>2</sup>	$6.9 \pm 1.1$ cm <sup>2</sup>	$-54.6 \pm 2.2$	10.3 cm <sup>2</sup>	$10.7 \pm 2.0$ cm <sup>2</sup>	$-28.5 \pm 3.5$
$^{18}\Delta\sigma^2$ II	6.6 cm <sup>2</sup>	$6.7 \pm 0.8$ cm <sup>2</sup>	$-54.9 \pm 1.7$	10.3 cm <sup>2</sup>	$10.5 \pm 1.2$ cm <sup>2</sup>	$-28.6 \pm 2.2$
$^{18}\Delta\sigma^2$ III	6.6 cm <sup>2</sup>	$5.5 \pm 0.3$ cm <sup>2</sup>	$-57.2 \pm 1.1$	10.3 cm <sup>2</sup>	$9.7 \pm 0.6$ cm <sup>2</sup>	$-30.0 \pm 1.4$
$^{17}\Delta\sigma^2$ I	7.5 cm <sup>2</sup>	$8.3 \pm 0.7$ cm <sup>2</sup>	$-53.7 \pm 1.4$	12.0 cm <sup>2</sup>	$12.2 \pm 2.0$ cm <sup>2</sup>	$-30.2 \pm 3.2$
$^{17}\Delta\sigma^2$ II	7.5 cm <sup>2</sup>	$7.5 \pm 0.5$ cm <sup>2</sup>	$-54.9 \pm 1.5$	12.0 cm <sup>2</sup>	$12.4 \pm 1.0$ cm <sup>2</sup>	$-28.3 \pm 1.7$
$\sigma_{18}^2/\sigma_{17}^2$	0.975	$0.960 \pm 0.027$	—————	0.977*	$0.993 \pm 0.035^*$	—————
$\sigma_{18}^2/\sigma_D^2$	1.24	$1.25 \pm 0.04$	$-56.6 \pm 11.1$	1.17	$1.17 \pm 0.03$	$-28.2 \pm 19.3$
$\sigma_{17}^2/\sigma_D^2$	1.28	$1.31 \pm 0.03$	$-62.8 \pm 7.0$	1.20	$1.18 \pm 0.04$	$-16.1 \pm 27$

Table 4.2: Simulations with synthetic data of a case A ( $T_{\text{sur}} = -55.0$  °C) and B ( $T_{\text{sur}} = -29.0$  °C). The diffusion lengths in the tabular are the firm diffusion lengths. Thus, this is before sampling, ice diffusion and thinning affected the input diffusion length. The estimated firm diffusion lengths are after correcting for sampling, ice diffusion and thinning (with their corresponding uncertainties).

reflect conditions as close as possible to present. As a result, the majority of the data sets presented here are from relatively shallow depths. This serves a twofold purpose. Firstly, it reduces the uncertainties regarding the ice flow that are considerably larger for the deeper parts of the core. Secondly, choosing to work with data sections as close to late Holocene conditions as possible, allows for a comparison of the estimated temperature to the site's present temperature. Although this is technically not a true comparison as the sites' surface temperatures have very likely varied during the Holocene, we consider it as a rough estimate of each techniques accuracy. For those cases where it was not possible to obtain late Holocene isotopic time series, due to limited data availability, we have used data originating from deeper sections of the ice cores with an age of about 10ka b2k reflecting conditions of the early Holocene. In Table 4.3 we provide relevant information for each data set as well as the present temperature and accumulation conditions for each ice core site.

The data sets were produced using a variety of techniques both with respect to the analysis itself (IRMS/CRDS), as well as with respect to the sample resolution and preparation (discrete/CFA). The majority of the data sets were analyzed using CRDS instrumentation. In particular the L1102i, L2120i and L2130i variants of the Picarro CRDS analyser were utilized for both discrete and CFA measurements of

$\delta^{18}\text{O}$  and  $\delta\text{D}$ . The rest of the data sets were analyzed using IRMS techniques with either  $\text{CO}_2$  equilibration or high temperature carbon reduction. For the case of the NEEM early Holocene data set, we work with two data sections that span the same depth interval and consist of discretely sampled and CFA measured data respectively. Additionally, the Dome C and Dome F data sections represent conditions typical for the East Antarctic Plateau and are sampled using a different approach (2.5 cm resolution discrete samples for the Dome C section and high resolution CFA measurements for the Dome F section).

In a way similar to the synthetic data test, we apply the various reconstruction techniques on every ice core data section. No reconstruction techniques involving  $\delta^{17}\text{O}$  are presented here due to lack of  $\delta^{17}\text{O}$  data. In order to achieve an uncertainty estimate for every reconstruction, we perform a sensitivity test that is based on  $N = 1000$  iterations. Assuming that every ice core section consists of  $J$   $\delta^{18}\text{O}$  and  $\delta\text{D}$  points, then a repetition is based on a data subsection with size  $J'$  that varies in the interval  $[J/2, J]$ . This “jittering” of the subsection size happens around the midpoint of every section and  $J'$  is drawn from a uniform distribution. Similar to the synthetic data tests, we also introduce uncertainties originating from the firn densification model, the ice flow model and ice diffusion (through the parameters:  $A$ ,  $\rho_{co}$ ,  $\rho_o$ ,  $P$ ,  $S$  and  $\sigma_{ice}$ ). For every reconstruction method and every ice core site, we calculate a mean and a standard deviation for the diffusion estimate, as well as a mean and a standard deviation for the temperature. Results are presented in Table 4.4. The estimated temperatures for ice cores covering the late-mid Holocene and early Holocene are shown in Fig. 4.2 and 4.3 respectively.

### 4.3 The fractionation factors

We also test how the choice of the parameterization of the isotope fractionation factors ( $\alpha_{18}$ ,  $\alpha_{\text{D}}$ ) influences the reconstructed temperatures of ice core sections. This is especially relevant for temperatures below  $-40^\circ\text{C}$ , as the confidence of the parameterized fractionation factors has been shown to be low for such cold temperatures (Ellehoj et al. 2013). The low confidence is partly a consequence of two things a) it is difficult to avoid kinetic fractionation in the measurement system and b) the water vapor pressure becomes small which makes it difficult to measure. The experiments are typically performed with a vapor source with a known isotopic composition that condenses out under controlled equilibrium conditions. For temperatures below  $-40^\circ\text{C}$ , single crystals have been observed growing against the flow of vapor in the tubes and chambers of the experimental setup (Ellehoj et al. 2013). This indicates that the water vapor experiences kinetic fractionation which disturbs the equilibrium process. In order to avoid this, most models generally extrapolate the warmer experiments to cover colder temperatures. Such extrapolations were performed in the parameterizations of Majoube (1970) ( $\alpha_{18}$ ) and Merlivat & Nief (1967) ( $\alpha_{\text{D}}$ ) which we used in the firn diffusivity parameterization (Appendix A). Their experiments were conducted down

to a minimum temperature of  $-33^{\circ}\text{C}$ , and then extrapolated to colder temperatures. Similarly, Ellehoj et al. (2013) estimated new values of  $\alpha_{18}$  and  $\alpha_{\text{D}}$  by measuring in the range  $-40^{\circ}\text{C}$  to  $0^{\circ}\text{C}$ . Their results showed a  $\alpha_{\text{D}}$  parameterization that deviated significantly from that of Merlivat & Nief (1967). A more recent study by Lamb et al. (2017) measured the value of  $\alpha_{\text{D}}$  in the range  $-87^{\circ}\text{C}$  to  $-39^{\circ}\text{C}$ . Their inferred equilibrium fractionation factors required a correction for kinetic effects. By including such a correction and extrapolating to warmer temperatures, they obtained a parameterization of  $\alpha_{\text{D}}$  with a slightly weaker temperature dependence than that of Merlivat & Nief (1967). Moreover, their  $\alpha_{\text{D}}$  deviated significantly from the results of Ellehoj et al. (2013). Such discrepancies between the fractionation factor parameterizations underline the importance of addressing how great an impact the potential inaccuracies have on the diffusion-based temperature proxy.

In this test, the procedure followed is common to that in Sec. 4.2 where a set of  $N = 1000$  repetitions is performed and both “jittering” of the data sets length and perturbation of input model variables takes place. The results are displayed in Fig. 4.4, where the temperatures resulting from the parameterizations of Majoube (1970) ( $\alpha_{18}$ ) and Merlivat & Nief (1967) ( $\alpha_{\text{D}}$ ) are compared to the temperatures resulting from the parameterizations of Ellehoj et al. (2013) ( $\alpha_{18}$ ,  $\alpha_{\text{D}}$ ) and Lamb et al. (2017) ( $\alpha_{\text{D}}$ ). In the latter case, the parameterization of  $\alpha_{18}$  from Majoube (1970) is used for the dual diffusion length methods.

## 5 DISCUSSION

### 5.1 Synthetic data

Based on the results of the sensitivity experiment with synthetic data, the following can be inferred. Firstly, the three techniques based on the single isotope diffusion, perform similarly and of all the techniques tested, yield the highest precision with a  $s_{\bar{T}} \approx 1.0^{\circ}\text{C}$  (the average precision  $s_{\bar{T}}$  of each technique is calculated by averaging the variances of all simulations). Additionally, the estimated temperatures  $\bar{T}$  are within  $1s_{\bar{T}}$  of the forcing temperature  $T_{\text{sur}}$ , a result pointing to a good performance with respect to the accuracy of the temperature estimation.

The precision of the differential diffusion techniques is slightly inferior to single diffusion with the subtraction technique being the least precise of all three differential diffusion approaches ( $s_{\bar{T}} \approx 2.6^{\circ}\text{C}$ ). A possible reason for this result may be the fact that the subtraction technique relies on the tuning of 8 optimization parameters as described in Sec. 3.1 and 3.2. Both the linear fit and the correlation techniques yield precision estimates of  $1.8^{\circ}\text{C}$  and  $1.3^{\circ}\text{C}$ , respectively. Despite the high precision of the correlation technique, the tests shows that the technique has a bias toward colder temperatures. The linear fit is therefore the most optimal of the differential diffusion techniques. All 10 experiments utilizing differential diffusion methods, yield an accuracy that lies within the  $2s_{\bar{T}}$  range ( $1s_{\bar{T}}$  range for 9 out of

Table 4.3: Ice core data sections and the corresponding drill site characteristic. Sources of data: (Steig et al. 2013)<sup>1</sup>, (Oerter et al. 2004)<sup>2</sup>, (Svensson et al. 2015)<sup>3</sup>, (Gkinis 2011)<sup>4</sup>, (Gkinis et al. 2011)<sup>5</sup>. Drill site characteristic sources: (Banta et al. 2008)<sup>a</sup>, (Oerter et al. 2004, Veres et al. 2013)<sup>b</sup>, (Watanabe et al. 2003, Kawamura et al. 2003)<sup>c</sup>, (Lorius et al. 1979)<sup>d</sup>, (NGRIP members 2004, Gkinis et al. 2014)<sup>e</sup>, (Johnsen et al. 2000)<sup>f</sup>, (Guillevic et al. 2013, Rasmussen et al. 2013)<sup>g</sup>.

Site Sections	Depth [m]	Age [kab2k]	Present T [°C]	A [m ice yr <sup>-1</sup> ]	P [Atm]	Thinning	Meas.	Analysis	$\Delta$ [cm]
GRIP mid <sup>f</sup>	753 – 776	3.7	–31.6	0.23	0.65	0.71	$\delta D, \delta^{18}O$	2130	2.5
GRIP late <sup>f</sup>	514 – 531	2.4	–31.6	0.23	0.65	0.79	$\delta D, \delta^{18}O$	2130	2.5
WAIS 2005A <sup>a,1</sup>	120 – 150	0.5	–31.1	0.22	0.77	0.97	$\delta^{18}O$	1102	5.0
EDML <sup>b,2</sup>	123 – 178	1.6	–44.6	0.08	0.67	0.93	$\delta D, \delta^{18}O$	IRMS	5.0
NEEM <sup>g</sup>	174 – 194	0.8	–29.0	0.22	0.72	0.31	$\delta D, \delta^{18}O$	2120	2.5
NGRIP <sup>e</sup>	174 – 194	0.9	–31.5	0.20	0.67	0.49	$\delta^{18}O$	IRMS	2.5
Dome F <sup>c,3</sup>	302 – 307	9.6	–57.3	0.04	0.61	0.93	$\delta D, \delta^{18}O$	CFA1102	0.5
Dome C <sup>d,4</sup>	308 – 318	9.9	–53.5	0.04	0.65	0.93	$\delta D, \delta^{18}O$	IRMS	2.5
GRIP early <sup>f</sup>	1449 – 1466	9.4	–31.6	0.23	0.65	0.42	$\delta D, \delta^{18}O$	2130	2.5
NEEM dis <sup>g,5</sup>	1380 – 1392	10.9	–29.0	0.22	0.72	0.31	$\delta D, \delta^{18}O$	2120	5.0
NEEM CFA <sup>g,5</sup>	1382 – 1399	10.9	–29.0	0.22	0.72	0.31	$\delta D, \delta^{18}O$	CFA1102	0.5
NGRIP I <sup>e</sup>	1300 – 1320	9.1	–31.5	0.18	0.67	0.55	$\delta^{18}O$	IRMS	5.0
NGRIP II <sup>e</sup>	1300 – 1320	9.1	–31.5	0.18	0.67	0.55	$\delta^{18}O$	IRMS	5.0

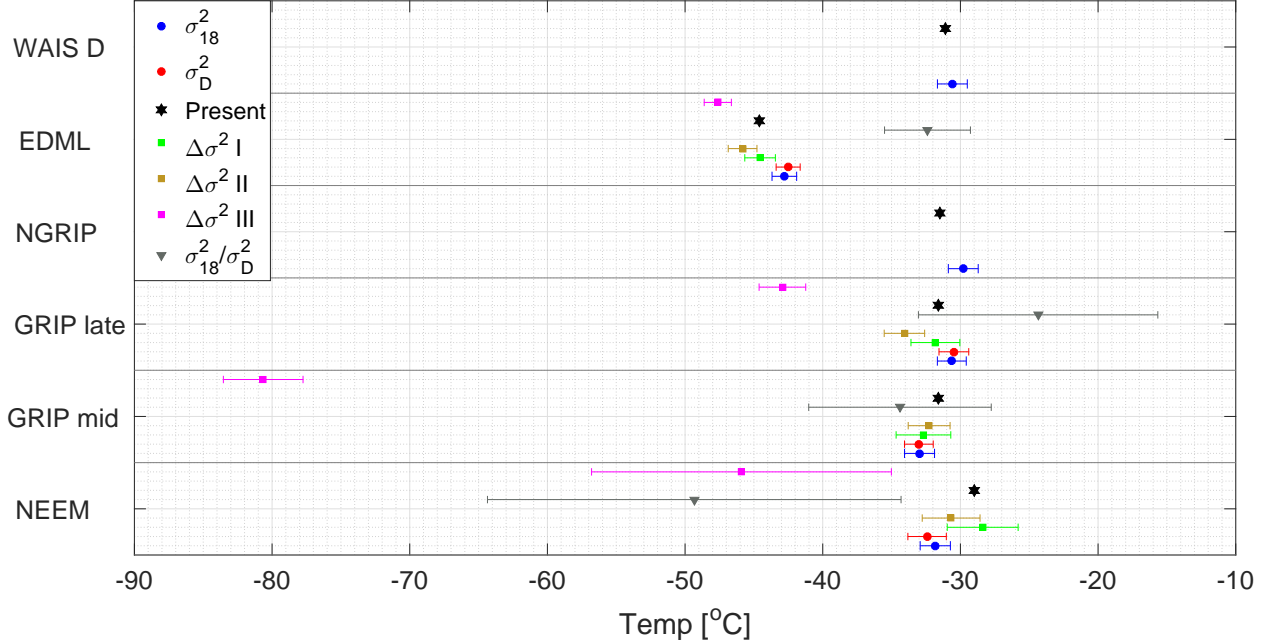


Figure 4.2: Late-mid Holocene section with reconstructed temperatures from the  $\sigma_{18}^2$  (blue circles),  $\sigma_D^2$  (red circles),  $\Delta\sigma^2$  I (green squares),  $\Delta\sigma^2$  II (brown squares),  $\Delta\sigma^2$  III (magenta squares) and  $\sigma_{18}^2/\sigma_D^2$  (grey triangles) methods. The black stars represent the present annual mean temperatures at the sites.

10 experiments). We can conclude that experiments involving the estimation of the diffusion length ratio indicate that the latter are practically unusable due to very high uncertainties with  $s_{\bar{T}}$  averaging to a value of  $\approx 16^\circ\text{C}$  for all four experiments. A general trend that seems to be apparent for all the experiments, is that the results for the case A forcing yield slightly lower uncertainties when compared to those for the case B forcing, likely indicating a temperature and accumulation influence in the performance of all the reconstruction techniques.

## 5.2 Ice core data

**5.2.1 The estimation of diffusion length from spectra:** From the spectra presented in Appendix F, we can see that the diffusion plus noise model (Eq. 3.2) provides good fits to the ice core data. For ice core sections with a resolution equal to (or higher than) 2.5 cm, we start seeing a difference in the spectral signature of the noise tail between the data from Greenland and Antarctica. The low accumulation Antarctic ice core sites seem to best represent the diffusion plus white noise model used in the synthetic data test. For instance, the PSD of Dome C in Fig. F.29 resembles well that of the synthetic data in Fig. 3.2, whereas a slightly more red noise tail is evident for the high accumulation sites on Greenland. We



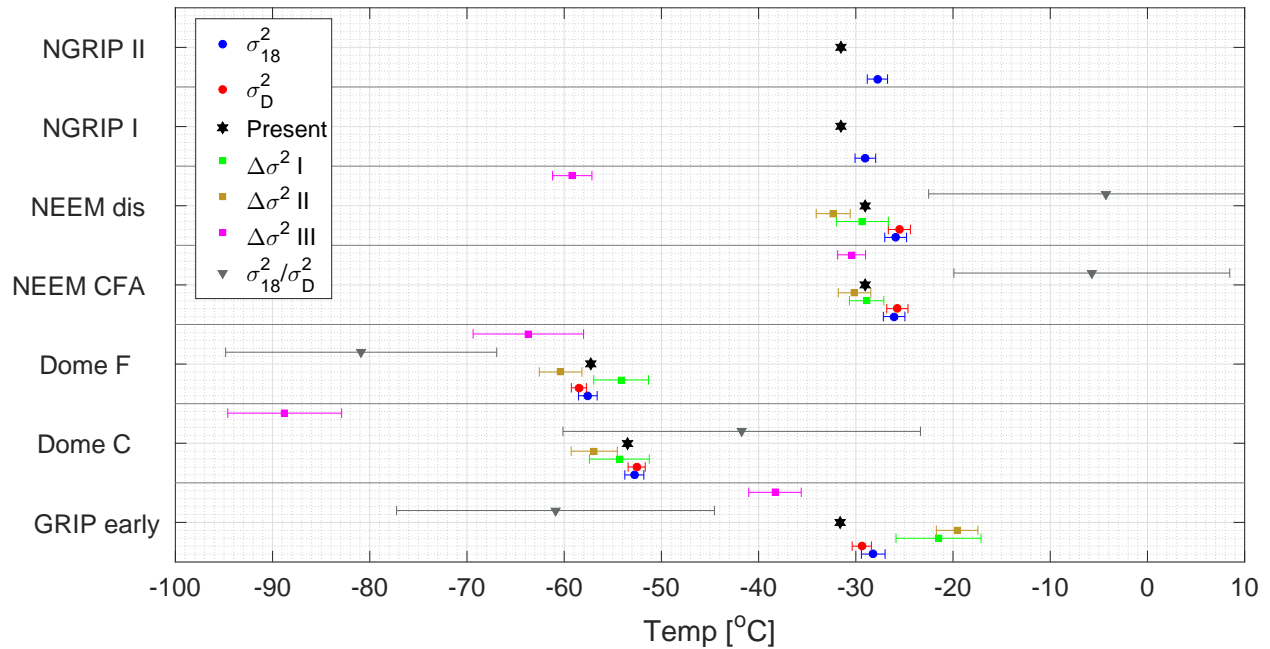


Figure 4.3: Early Holocene section with reconstructed temperatures from the  $\sigma_{18}^2$  (blue circles),  $\sigma_D^2$  (red circles),  $\Delta\sigma^2$  I (green squares),  $\Delta\sigma^2$  II (brown squares),  $\Delta\sigma^2$  III (magenta squares) and  $\sigma_{18}^2/\sigma_D^2$  (grey triangles) methods. The black stars represent the present annual mean temperatures at the sites.

don't know why the noise for some of the Greenlandic sites behaves differently, but the white noise of the Antarctic ice core data coincides well with isotopic signals that likely comprise of a few events per year and is whiten due to post depositional effects such as snow relocation. Nonetheless, The AR-1 noise model in Eq. 3.2 describes both the red and white noise well.

An example of how sample resolution plays a role in assessing the value of the estimated diffusion length, can be seen when visually comparing the spectra of the NEEM early Holocene data in Fig. F.5 and F.8. The lack of sufficient resolution in Fig F.8 (discrete 5 cm data) results in a poorly resolved noise signal. On the contrary, the 0.5 cm resolution of the CFA obtained data (both datasets are from approximately the same depth interval) allows for a much better insight into the noise characteristics of the isotopic time series and therefore a more robust diffusion length estimation. Despite differences in the resolution of the power spectra, the fitting procedure provides similar estimates of the firm diffusion lengths as seen in Table 4.4. This result indicates that even though the diffusion length can be estimated with less certainty, the diffusion length is still preserved in the signal which underlines how powerful a technique the spectral estimation of diffusion length is.

Table 4.4: Ice core results with the estimated firn diffusion lengths and their corresponding temperatures [°C]. The units for the  $\sigma_{18}$  and the  $\sigma_D$  values are expressed in cm and the unit for  $^{18}\Delta\sigma^2$  is expressed in  $\text{cm}^2$ .

Site Name	$\sigma_{18}$	$\sigma_D$	$^{18}\Delta\sigma^2$ I	$^{18}\Delta\sigma^2$ II	$^{18}\Delta\sigma^2$ III	$\sigma_{18}^2/\sigma_D^2$
GRIP mid	$7.83 \pm 0.17 \text{ cm}$	$7.20 \pm 0.16 \text{ cm}$	$9.4 \pm 1.0 \text{ cm}^2$	$9.6 \pm 0.7 \text{ cm}^2$	$0.2 \pm 0.1 \text{ cm}^2$	$1.18 \pm 0.02$
	$-33.0 \pm 1.1 ^\circ\text{C}$	$-33.0 \pm 1.0 ^\circ\text{C}$	$-32.7 \pm 2.0 ^\circ\text{C}$	$-32.3 \pm 1.5 ^\circ\text{C}$	$-80.6 \pm 2.9 ^\circ\text{C}$	$-34.4 \pm 6.6 ^\circ\text{C}$
GRIP late	$8.52 \pm 0.12 \text{ cm}$	$7.92 \pm 0.16 \text{ cm}$	$9.9 \pm 0.8 \text{ cm}^2$	$8.6 \pm 0.5 \text{ cm}^2$	$4.8 \pm 0.5 \text{ cm}^2$	$1.16 \pm 0.02$
	$-30.6 \pm 1.1 ^\circ\text{C}$	$-30.5 \pm 1.1 ^\circ\text{C}$	$-31.8 \pm 1.8 ^\circ\text{C}$	$-34.1 \pm 1.5 ^\circ\text{C}$	$-43.0 \pm 1.7 ^\circ\text{C}$	$-24.4 \pm 8.7 ^\circ\text{C}$
WAIS 2005A	$7.05 \pm 0.11 \text{ cm}$	—————	—————	—————	—————	—————
	$-31.7 \pm 1.1 ^\circ\text{C}$	—————	—————	—————	—————	—————
EDML	$7.72 \pm 0.09 \text{ cm}$	$7.12 \pm 0.08 \text{ cm}$	$8.9 \pm 0.3 \text{ cm}^2$	$8.1 \pm 0.3 \text{ cm}^2$	$7.1 \pm 0.2 \text{ cm}^2$	$1.18 \pm 0.01$
	$-42.8 \pm 0.9 ^\circ\text{C}$	$-42.5 \pm 0.9 ^\circ\text{C}$	$-44.6 \pm 1.1 ^\circ\text{C}$	$-45.9 \pm 1.0 ^\circ\text{C}$	$-47.6 \pm 1.0 ^\circ\text{C}$	$-32.4 \pm 3.1 ^\circ\text{C}$
NEEM	$7.98 \pm 0.22 \text{ cm}$	$7.20 \pm 0.32 \text{ cm}$	$11.8 \pm 1.6 \text{ cm}^2$	$10.2 \pm 1.1 \text{ cm}^2$	$4.5 \pm 2.0 \text{ cm}^2$	$1.23 \pm 0.05$
	$-31.8 \pm 1.1 ^\circ\text{C}$	$-32.4 \pm 1.4 ^\circ\text{C}$	$-28.4 \pm 2.6 ^\circ\text{C}$	$-30.7 \pm 2.1 ^\circ\text{C}$	$-45.9 \pm 10.1 ^\circ\text{C}$	$-49.3 \pm 15.0 ^\circ\text{C}$
NGRIP	$9.24 \pm 0.20 \text{ cm}$	—————	—————	—————	—————	—————
	$-29.8 \pm 1.1 ^\circ\text{C}$	—————	—————	—————	—————	—————
Dome F	$5.76 \pm 0.15 \text{ cm}$	$4.92 \pm 0.06 \text{ cm}$	$9.0 \pm 1.8 \text{ cm}^2$	$5.4 \pm 0.8 \text{ cm}^2$	$4.4 \pm 1.9 \text{ cm}^2$	$1.37 \pm 0.08$
	$-57.6 \pm 1.0 ^\circ\text{C}$	$-58.5 \pm 0.8 ^\circ\text{C}$	$-54.2 \pm 2.8 ^\circ\text{C}$	$-60.4 \pm 2.2 ^\circ\text{C}$	$-63.7 \pm 5.7 ^\circ\text{C}$	$-80.9 \pm 14.0 ^\circ\text{C}$
Dome C	$6.97 \pm 0.15 \text{ cm}$	$6.34 \pm 0.08 \text{ cm}$	$8.4 \pm 1.9 \text{ cm}^2$	$6.7 \pm 1.1 \text{ cm}^2$	$0.4 \pm 0.4 \text{ cm}^2$	$1.21 \pm 0.05$
	$-52.8 \pm 1.0 ^\circ\text{C}$	$-52.5 \pm 0.9 ^\circ\text{C}$	$-54.3 \pm 3.0 ^\circ\text{C}$	$-56.9 \pm 2.3 ^\circ\text{C}$	$-88.8 \pm 5.9 ^\circ\text{C}$	$-42.8 \pm 18.4 ^\circ\text{C}$
GRIP early	$9.31 \pm 0.24 \text{ cm}$	$8.25 \pm 0.09 \text{ cm}$	$18.7 \pm 4.0 \text{ cm}^2$	$20.4 \pm 1.9 \text{ cm}^2$	$6.6 \pm 1.1 \text{ cm}^2$	$1.27 \pm 0.06$
	$-28.2 \pm 1.2 ^\circ\text{C}$	$-29.4 \pm 1.0 ^\circ\text{C}$	$-21.5 \pm 4.4 ^\circ\text{C}$	$-19.6 \pm 2.1 ^\circ\text{C}$	$-38.4 \pm 2.7 ^\circ\text{C}$	$-60.9 \pm 16.4 ^\circ\text{C}$
NEEM dis	$10.33 \pm 0.19 \text{ cm}$	$9.72 \pm 0.20 \text{ cm}$	$12.1 \pm 1.8 \text{ cm}^2$	$10.0 \pm 0.9 \text{ cm}^2$	$1.6 \pm 0.2 \text{ cm}^2$	$1.13 \pm 0.02$
	$-25.9 \pm 1.1 ^\circ\text{C}$	$-25.5 \pm 1.1 ^\circ\text{C}$	$-29.3 \pm 2.7 ^\circ\text{C}$	$-32.3 \pm 1.8 ^\circ\text{C}$	$-59.2 \pm 2.0 ^\circ\text{C}$	$-4.2 \pm 18.3 ^\circ\text{C}$
NEEM CFA	$10.27 \pm 0.19 \text{ cm}$	$9.65 \pm 0.18 \text{ cm}$	$12.3 \pm 1.1 \text{ cm}^2$	$11.4 \pm 0.9 \text{ cm}^2$	$11.2 \pm 0.6 \text{ cm}^2$	$1.13 \pm 0.01$
	$-26.1 \pm 1.1 ^\circ\text{C}$	$-25.7 \pm 1.1 ^\circ\text{C}$	$-29.0 \pm 1.8 ^\circ\text{C}$	$-30.1 \pm 1.7 ^\circ\text{C}$	$-30.4 \pm 1.4 ^\circ\text{C}$	$-5.7 \pm 14.2 ^\circ\text{C}$
NGRIP I	$9.68 \pm 0.16 \text{ cm}$	—————	—————	—————	—————	—————
	$-29.0 \pm 1.1 ^\circ\text{C}$	—————	—————	—————	—————	—————
NGRIP II	$10.14 \pm 0.17 \text{ cm}$	—————	—————	—————	—————	—————
	$-27.8 \pm 1.0 ^\circ\text{C}$	—————	—————	—————	—————	—————

In this study, the annual peak is removed in five out of thirteen cases. However, we do not see any distinguished multiannual variability manifested as spectral peaks. A correction similar to that of the annual peak filter is therefore not implemented. This does not necessarily mean that there is no imprint in those bands to start with, but our analysis does not indicate this and these signals are either too weak to noticeably affect the fits of the assumed model (i.e. diffusion plus noise) or they cannot be resolved at all because their power lies lower than the measurement noise.

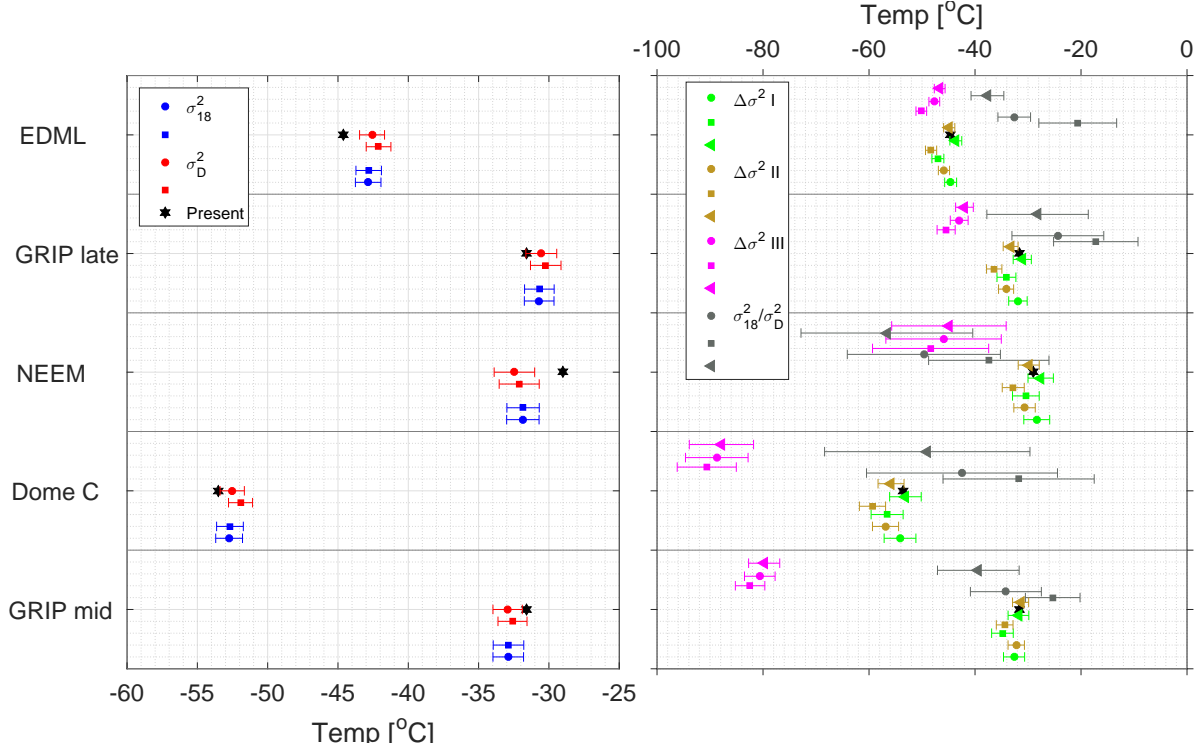


Figure 4.4: Temperature reconstructions based on different fractionation factor parameterizations. The left figure shows the single isotopologue methods and the right figure shows the dual isotope methods. Circles correspond to fractionation factors from Majoube (1970), Merlivat & Nief (1967), squares correspond to fractionation factors from Ellehoj et al. (2013) and triangles from Lamb et al. (2017), Majoube (1970).

5.2.2 *The temperature reconstructions:* The precision  $s_{\bar{T}}$  of each reconstruction technique has been quantified by averaging the variances of the reconstructed temperatures (Table 4.4). In accordance with the results from the synthetic data test, the most precise reconstructions are obtained when using the single isotope diffusion methods. The single diffusion methods have a  $s_{\bar{T}}$  of 1.1 °C, while the differential diffusion methods  $^{18}\Delta\sigma^2$  I, II and III have a  $s_{\bar{T}}$  of 2.6 °C, 1.9 °C and 4.8 °C, respectively. The correlation-based technique is hereby shown to be the least precise differential diffusion method. This differs from the result of the synthetic data, where the correlation-based technique had the most precise results. Of the differential diffusion methods, the linear fit of the logarithmic ratio provides the most precise results, with a precision similar to that found from the synthetic data (Sec. 5.1). Of all the tested techniques, the diffusion length ratio method is the least precise with a  $s_{\bar{T}}$  of 11.8 °C. A similar precision was found from the synthetic data.

The perturbations of the model parameters help achieve a realistic view on the overall precision and

it facilitates a comparison between the single and the differential diffusion techniques. Nonetheless, we want to emphasize that the presented precisions do not represent the absolute obtainable precision of the diffusion-based temperature reconstruction techniques. While the uncertainties presented in Table 4.1 represents typical Holocene values estimated for Central Greenland and the East Antarctic Ice Cap, the input parameters' uncertainties in the firn diffusion model are essentially both depth and site dependent. For instance, we have a better knowledge about the ice flow thinning at a low accumulation site e.g. Dome C compared to that of a high accumulation site e.g. NGRIP for early Holocene ice core data, This is a result of the Dome C site's early Holocene period being at a depth of 300 m while the NGRIP site's early Holocene period is at a depth of 1300 m. Additionally, it is more more difficult to estimate the glacial accumulation rate at sites where the present day values already are very low. Basically, inferring a change between 3 cm/yr and 1.5 cm/yr (and how stable this 1.5 cm/yr estimate is during the glacial) is much harder and with higher uncertainties compared to going from 23 cm/yr to 10 cm/yr (where annual layer thickness information is available from chemistry). Similarly,  $\rho_{co}$  and  $\rho_o$  are better known for Holocene conditions and likely close to present day values while glacial conditions represent a regime at which those values may change more considerably. Thus, when utilizing the diffusion techniques on long ice core records, we propose that the uncertainties of such model parameters and corrections should be based on specific characteristics of the ice core site and the part (or depth) of the core under consideration.

It is not possible to quantify the accuracy of the methods when applied on short ice core data sections, as the reconstructed temperatures represent the integrated firn column temperature. Even though the firn diffusion model has a polythermal firn layer due to the seasonal temperature variation, we can only estimate a single value of the diffusion length from the data (the exact temperature gradients a layer has experienced is unknown). The reconstructed temperatures should therefore not necessarily be completely identical to present day annual temperatures. However, clear outliers can still be inferred from the data as Holocene temperature estimates that deviate with 30 °C from the present day annual mean temperatures are unrealistic.

First we address the correlation-based and diffusion length ratio techniques as these two methods result in temperatures that clearly deviate with present day annual mean temperatures (Fig. 4.2 and 4.3). Besides the low precision of the diffusion length ratio method, temperature estimates using the the correlation-based and diffusion length ratio techniques are highly inconsistent with the results of the other techniques, with root-mean-square deviations (RMSD) varying from 21 °C to 34 °C. In addition, it can be seen that the correlation-based method results in significantly different temperatures for the discretely and continuously measured NEEM section. A similar difference is not found from the spectral-based methods. Instead, these provide consistent temperatures independent of the processing scheme. The generally poor performance of

the correlation-based method on ice core data contradicts the high accuracy and precision of the synthetic reconstructions, and is most likely caused by an oversimplification of the relationship between  $\delta D$  and  $\delta^{18}O$ . The generation of the synthetic data is based on the assumption that  $\delta D = 8 \cdot \delta^{18}O + 10\text{‰}$ . However, this premise neglects the time dependent  $d_{xs}$  signal. The correlation-based method can therefore be used to accurately reconstruct synthetic temperatures, while the accuracy and precision are much lower for ice core data, as such data has been influenced by the  $d_{xs}$  signal. In addition, these temperature estimates have been shown to be dependent on the sampling process. The correlation-based method therefore yields uncertain estimates of the differential diffusion length.

The temperature estimates originating from the  $\sigma_{18}^2$  and  $\sigma_D^2$  methods are found to have a RMSD of  $0.7^\circ\text{C}$ . This shows that the  $\sigma_{18}^2$  and  $\sigma_D^2$  methods result in similar temperatures, which is consistent with the high accuracies found from the synthetic data test. Furthermore, the early Holocene ice core data from Greenland consistently shows reconstructed temperatures warmer than present day (Fig. 4.3), which corresponds well with a HCO of around  $3^\circ\text{C}$  warming as found by Dahl-Jensen et al. (1998), Vinther et al. (2009). With the exception of WAIS D, the estimated temperatures for the late-mid Holocene using the  $\sigma_{18}^2$  and  $\sigma_D^2$  methods are either slightly warmer or colder than present day (Fig. 4.2). These sections represent ages ranging from 0.9 to 3.7 ka and it is not unreasonable to assume that the sites' surface temperatures have varied in time. We emphasize that some of the presented ice core sections are as short as 15 m, and that such temperature estimates will potentially be more similar to present day when averaged over a long time series.

The temperature estimates of the  $^{18}\Delta\sigma^2$  I method are similar to the present day annual temperature in six out of nine cases. However, the results of the  $^{18}\Delta\sigma^2$  I and II techniques have a RMSD of  $3.8^\circ\text{C}$ . The seemingly accurate performance of the  $^{18}\Delta\sigma^2$  I method could be either a coincidence or correct. Two of the similar temperature results are from the NEEM early Holocene data that likely should have had warmer surface temperatures than present day. It is therefore difficult to select the most accurate results as both of the differential diffusion techniques before performed well in the accuracy test with the synthetic data. One should therefore not have a preferred technique without utilizing both methods on longer ice core sections. Basically, the reconstructed temperatures could be similar when the temperatures have been averaged over a longer record. Besides the internal differences in the results of the differential techniques, most of the temperature estimates do not match the results of the single diffusion lengths.

### 5.3 The fractionation factors

The temperature estimates resulting from the different fractionation factor parametrizations are shown in Fig. 4.4. For each method, the influence of the choice of parametrization on the reconstructed temperatures

has been quantified by calculating the RMSD between temperature estimates of two parametrizations. Comparing the parametrizations of Ellehoj et al. (2013) to those of Majoube (1970) and Merlivat & Nief (1967), the RMSDs of reconstructions that are based on the single diffusion lengths  $\sigma_{18}^2$  and  $\sigma_D^2$  are  $0.04^\circ\text{C}$  and  $0.4^\circ\text{C}$ . Thus, it is evident that the choice of fractionation factors has an insignificant effect on the results of the  $\sigma_{18}^2$  method and a small effect on the results of the  $\sigma_D^2$  method. The choice of parameterization has a greater effect on the temperatures of the  $^{18}\Delta\sigma^2$  techniques, where the temperature estimate of the  $^{18}\Delta\sigma^2$  I, II and III techniques have RMSDs of  $2.3^\circ\text{C}$ ,  $2.3^\circ\text{C}$  and  $2.2^\circ\text{C}$ , respectively. Comparing the parametrization of Lamb et al. (2017) to that of Merlivat & Nief (1967), the temperatures of the  $^{18}\Delta\sigma^2$  I, II and III techniques have RMSDs of  $0.9^\circ\text{C}$ ,  $0.9^\circ\text{C}$  and  $1.0^\circ\text{C}$ , respectively. In general, smaller RMSDs are found when comparing with temperature estimates based on the Lamb et al. (2017) parametrization. For instance, comparing the temperatures of the  $\sigma_{18}^2/\sigma_D^2$  technique based on Lamb et al. (2017) with those of Merlivat & Nief (1967), the  $\sigma_{18}^2/\sigma_D^2$  technique yields a RMSD of  $5.9^\circ\text{C}$ , while the RMSD is  $11.0^\circ\text{C}$  when comparing the results based on the parametrizations of Ellehoj et al. (2013) with those of Majoube (1970) and Merlivat & Nief (1967). There are two reasons to why the RMSDs are smaller when comparing with the Lamb et al. (2017) parametrization: the parametrized  $\alpha_D$  of Merlivat & Nief (1967) differs more with that of Ellehoj et al. (2013) than with that of Lamb et al. (2017), and the same  $\alpha_{18}$  parametrization is used when comparing with Lamb et al. (2017).

The  $\sigma_{18}^2/\sigma_D^2$  method is significantly more influenced by the fractionation factors. The high RMSDs imply that even if the diffusion length ratio is estimated with high confidence, the method is still too sensitive to the choice of parameterization. This makes the method less suitable as a paleoclimatic thermometer.

#### 5.4 Outlook with respect to ice core measurements

It is obvious from the analysis we present here that the type of isotopic analysis chosen has an impact on the quality of the power spectral estimates and subsequently on the diffusion length estimation. One such important property of the spectral estimation that is directly dependent on the nature of the isotopic analysis is the achievable Nyquist frequency, defined by the sampling resolution  $\Delta$  of the isotopic time series. The value of the Nyquist frequency  $f_{Nq}$  sets the limit in the frequency space until which a power spectral estimate can be obtained. The higher the value of  $f_{Nq}$ , the more likely it is that the noise part  $|\hat{\eta}(k)|^2$  of the power spectrum will be resolved by the spectral estimation routine. The deeper the section under study, the higher the required  $f_{Nq}$  due to the fact that the ice flow thinning results in a progressively lower value for the diffusion length and as a result the diffusion part of the spectrum extends more into the higher frequencies. This effect manifests particularly in the case of the early Holocene Greenland

sections of this study. For the case of the NEEM early Holocene record, one can observe the clear benefit of the higher sampling resolution by comparing the discrete ( $\Delta = 5$  cm) to the the CFA ( $\Delta = 0.5$  cm) data set. Characterizing the noise signal  $|\hat{\eta}(k)|^2$  is more straight forward in the case of the CFA data. On the contrary, at these depths of the NEEM core, the resolution of 5 cm results in the spectral estimation not being able to resolve the noise signal.

The diffusion of the sampling and measurement process itself is a parameter that needs to be thoroughly addressed particularly during the development and construction of a CFA system as well as during the measurement of an ice core with such a system. Ideally, one would aim for (a) a dispersive behavior that resembles as close as possible that of Gaussian mixing, (b) a measurement system diffusion length  $\sigma_{cfa}$  that is as low as possible and (c) a diffusive behavior that is stable as a function of time. Real measurements with CFA systems indicate that most likely due to surface effects in the experimental apparatus that lead to sample memory, the transfer functions of such systems depart from the ideal model of Gaussian dispersion showing a slightly skewed behavior. For some systems, this behavior resembles more that of a slightly skewed Log-Normal distribution (Gkinis et al. 2011, Maselli et al. 2013, Emanuelsson et al. 2015) or a more skewed distribution that in the case of Jones et al. (2017) requires the product of two Log-Normal distributions to be accurately modeled. The result of this behavior to the power spectral density is still a matter of further study as high resolution datasets obtained with CFA systems are relatively recent.

Additionally the accuracy of the depth registration is essential in order for accurate spectral estimates to be possible. Instabilities in melt rates of the ice stick under consideration can in principle be addressed and a first-order correction can be available assuming a length encoder is installed in the system. Such a correction though does not take into account the fact that due to the constant sample flow rate through the CFA system, the constant mixing volume of the system's components (sample tubing, valves etc) will cause a variable mixing as melt rates change. The magnitudes and importance of these variations are not easy to assess and more work will be required in the future in order to characterize and correct for these effects.

Due to the recent advances in laser spectroscopy we expect measurements of the  $\delta^{17}\text{O}$  signal to be a common output from analyzed ice cores. As we showed with synthetic data, such a signal can also be used to reconstruct temperatures. Especially the differential diffusion length of  $\delta^{17}\text{O}$  and  $\delta\text{D}$  showed higher precision than that of  $\delta^{18}\text{O}$  and  $\delta\text{D}$ . Such measurements however, require that laboratories around the world have access to well calibrated standards. Calibration protocols for  $\delta^{17}\text{O}$  have been suggested (Schoenemann et al. 2013) although there is still a lack of  $\delta^{17}\text{O}$  values for the International Atomic Energy Agency standards VSMOW (Vienna Standard Mean Ocean Water) and SLAP (Standard Light

Antarctic Precipitation).

## 6 CONCLUSIONS

This study assessed the performance of six different diffusion-based temperature reconstruction techniques. By applying the methods on synthetic data, first order tests of accuracy and bias were demonstrated and evaluated. Moreover, this approach facilitated precision estimates of each method. The precision of each technique was further quantified by utilizing every variety of the diffusion-based temperature proxy on thirteen high resolution data sets from Greenland and Antarctica. The results showed that the single diffusion length methods yielded similar temperatures and that they are the most precise of all the presented reconstruction techniques. The most precise of the three differential diffusion length techniques was the linear fit of the logarithmic ratio. The most uncertain way of reconstructing past temperatures was by employing the diffusion length ratio method. The results from the correlation-based method were inconsistent to the results obtained through the spectral-based methods, and the method was considered to yield uncertain estimates of the differential diffusion length.

It was furthermore shown that the choice of fractionation factor parametrization only had a small impact on the results from the single diffusion length methods, while the influence was slightly higher for the differential diffusion length methods. The diffusion length ratio method was highly sensitive to the fractionation factor parametrization, and the method is not suitable as a paleoclimatic thermometer.

In conclusion, despite that the dual diffusion techniques seem to be the more optimal choices due to their independence of sampling and ice diffusion or densification and thinning processes, the uncertain estimates should outweigh the theoretical advantages for Holocene ice core data.

## ACKNOWLEDGEMENTS

The research leading to these results has received funding from the European Research Council under the European Union's Seventh Framework Programme (FP7/2007-2013) grant agreement #610055 as part of the ice2ice project. The authors acknowledge the support of the Danish National Research Foundation through the Centre for Ice and Climate at the Niels Bohr Institute (Copenhagen, Denmark). We would like to thank A. Schauer, S. Schoenemann, B. Markle and E. Steig for ongoing fruitful discussions and inspiration through the years on all things related to water isotope analysis and modelling. We thank our colleagues at Centre for Ice and Climate for their generous contribution, especially those who have assisted in processing the ice cores. We also thank the NEEM project for providing the NEEM ice core samples. NEEM is directed and organized by the Center of Ice and Climate at the Niels Bohr Institute and US NSF, Office of Polar Programs. It is supported by funding agencies and institutions in



Belgium (FNRS-CFB and FWO), Canada (NRCan/GSC), China (CAS), Denmark (FIST), France (IPEV, CNRS/INSU, CEA and ANR), Germany (AWI), Iceland (RannIs), Japan (NIPR), Korea (KOPRI), The Netherlands (NWO/ALW), Sweden (VR), Switzerland (SNF), United Kingdom (NERC) and the USA (US NSF, Office of Polar Programs).

#### CO-AUTHORSHIP

CH and VG contributed equally to this work.

#### APPENDIX A

##### FIRN DIFFUSIVITY

We express the diffusivity as a function of firn density  $\rho$  and we use (Johnsen et al. 2000):

$$D(\rho) = \frac{m p D_{ai}}{R T \alpha_i \tau} \left( \frac{1}{\rho} - \frac{1}{\rho_{ice}} \right). \quad (\text{A.1})$$

The terms used in Eq. (A.1) and the parametrization used for them are described below:

- m: molar weight (kg)
- p: saturation vapor pressure over ice (Pa). We use (Murphy & Koop 2006):

$$p = \exp \left( 9.5504 - \frac{5723.265}{T} + 3.530 \ln(T) - 0.0073 T \right) \quad (\text{A.2})$$

- $D_{ai}$ : diffusivity of water vapor (for isotopologue  $i$ ) in air ( $\text{m}^2\text{s}^{-1}$ ). For the diffusivity of the abundant isotopologue water vapor  $D_a$  we use (Hall & Pruppacher 1976):

$$D_a = 2.1 \cdot 10^{-5} \left( \frac{T}{T_o} \right)^{1.94} \left( \frac{P_o}{P} \right) \quad (\text{A.3})$$

with  $P_o = 1 \text{ Atm}$ ,  $T_o = 273.15 \text{ K}$  and  $P$ ,  $T$  the ambient pressure (Atm) and temperature (K).

Additionally from Merlivat & Jouzel (1979)  $D_{a^2\text{H}} = 0.9755 D_a$  and  $D_{a^{18}\text{O}} = 0.9723 D_a$  and from

Barkan & Luz (2007)  $D_{a^{17}\text{O}} = 0.98555 D_a$ .

- R: molar gas constant  $R = 8.3144 \text{ (m}^3\text{PaK}^{-1}\text{mol}^{-1}\text{)}$
- T: Ambient temperature (K)
- $\alpha_i$ : Ice – Vapor fractionation factor. we use the formulations by Majoube (1970), Merlivat & Nief (1967) and Barkan & Luz (2005) for  $\alpha_{s/v}^2$ ,  $\alpha_{s/v}^{18}$  and  $\alpha_{s/v}^{17}$  respectively.

$$\alpha_{\text{Ice/Vapor}}(^2\text{H}/^1\text{H}) = 0.9098 \exp(16288/T^2) \quad (\text{A.4})$$

$$\alpha_{\text{Ice/Vapor}}(^{18}\text{O}/^{16}\text{O}) = 0.9722 \exp(11.839/T) \quad (\text{A.5})$$

$$\alpha_{\text{Ice/Vapor}}(^{17}\text{O}/^{16}\text{O}) = \exp(0.529 \ln[\alpha_{\text{Ice/Vapor}}(^{18}\text{O}/^{16}\text{O})]) \quad (\text{A.6})$$

- $\tau$ : The firn tortuosity. We use Schwander et al. (1988) as in Johnsen et al. (2000). More recent results include Freitag et al. (2002) and Adolph & Albert (2014).

$$\frac{1}{\tau} = 1 - b \cdot \left( \frac{\rho}{\rho_{\text{ice}}} \right)^2 \quad \rho \leq \frac{\rho_{\text{ice}}}{\sqrt{b}}, \quad b = 1.3 \quad (\text{A.7})$$

Based on Eq. (A.7),  $\tau \rightarrow \infty$  for  $\rho > 804.3 \text{ kg m}^{-3}$

## APPENDIX B

### THE FIRN TEMPERATURE PROFILE

Temperature variations in the firn column affect the amount of firn diffusion. The temperature profile  $T$  is modeled by solving the general heat transfer equation:

$$\frac{\partial T}{\partial t} = \kappa \frac{\partial^2 T}{\partial z^2} - \left( w - \left( \frac{\kappa}{\rho} + \frac{\partial \kappa}{\partial \rho} \right) \frac{\partial \rho}{\partial z} \right) \frac{\partial T}{\partial z}, \quad (\text{B.1})$$

where  $\rho$  is the density,  $w$  is the vertical velocity and  $\kappa$  is the thermal diffusivity of firn. Here the internal heat production and the heat transport in the horizontal plane have been neglected. The thermal diffusivity of firn depends on density and the thermal diffusivity of ice ( $\kappa_{\text{ice}}$ ) (Schwander et al. 1997):

$$\kappa = \kappa_{\text{ice}} \left( \frac{\rho}{\rho_i} \right)^{1-0.5(\rho/\rho_i)}, \quad (\text{B.2})$$

where  $\rho_i$  is the density of ice. The thermal diffusivity of ice is defined as (Cuffey & Paterson 2010):

$$\kappa_{\text{ice}} = \frac{k}{\rho_i c_p} = \frac{9.828 \cdot \exp(-5.7 \cdot 10^{-3} T) \cdot 3.16 \cdot 10^7}{\rho_i (152.5 + 7.122 T)}, \quad (\text{B.3})$$

where  $c_p$  is the specific heat capacity and  $k$  is the thermal conductivity of ice. This allows for the computation of changes in thermal diffusivity with density:

$$\frac{\partial \kappa}{\partial \rho} = \kappa \left( \frac{1}{\rho} - \frac{1}{2\rho_i} \right) \left( 1 + \ln \left( \frac{\rho}{\rho_i} \right) \right). \quad (\text{B.4})$$

The surface temperature is parameterized as fluctuations around the mean annual temperature ( $T_{\text{mean}}$ ) as in Simonsen et al. (2011):

$$T_{\text{surf}}(t) = T_{\text{mean}} + A \cos(bt) + B \cos(2bt), \quad (\text{B.5})$$

where  $A = 16.5$ ,  $B = 3.0$  and  $b = 0.5236$  are constants controlling the temperature amplitude and narrowness of the summer peak.

Figure B.1 shows the temperature variation a snow package experiences as it moves downwards. The seasonal temperature variation penetrates down to a depth of 10 – 12 m. The heat equation is solved numerically by using a Crank-Nicolson scheme (Durrant 2010).

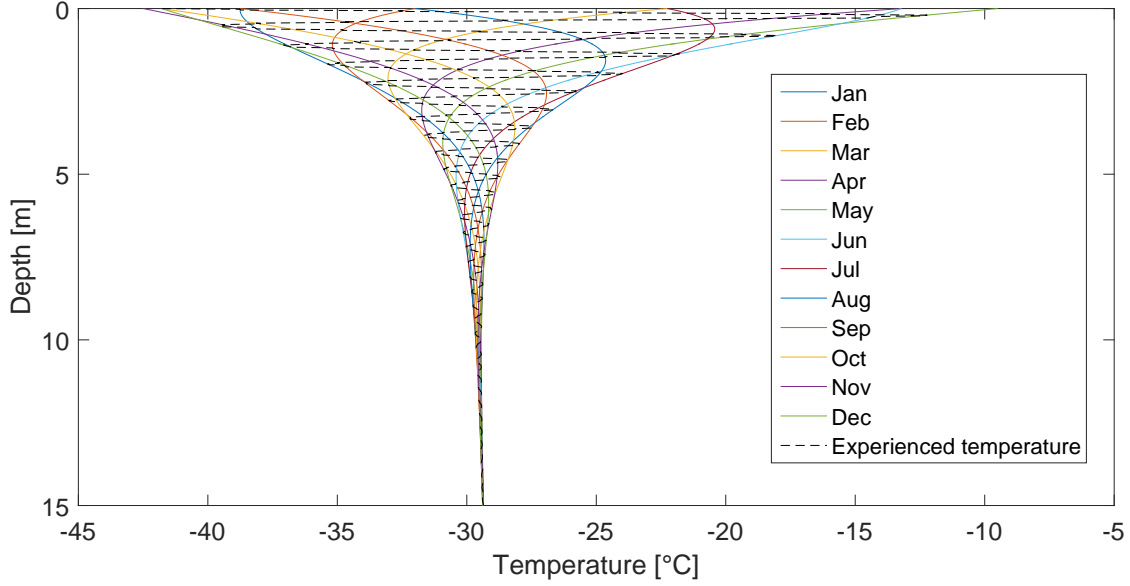


Figure B.1: Each solid colored line represent the temperature in one month of a year. The temperature a snow layer experiences as it moves down through the snow is represented by the black dashed line. The temperature is constant around 10-12 m.  $T_{\text{mean}} = -29^\circ\text{C}$ ,  $A = 0.22 \text{ myr}^{-1}$  ice. eq.

## APPENDIX C

### ICE DIFFUSIVITY

The solid ice diffusivity parametrization we use in this study is based on Ramseier (1967) as it is consistent with previous studies. In this section we provide the reader with parametrizations from other studies. We assume an Arrhenius type relationship for the ice diffusivity of the form:

$$D_{\text{ice}} = D_o \exp\left(-\frac{X}{T}\right) [\text{m}^2\text{s}^{-1}]. \quad (\text{C.1})$$

In Eq. C.1,  $D_o$  is the pre-exponential factor in  $\text{m}^2\text{s}^{-1}$  and  $X$  is the Arrhenius coefficient where  $X = Q/R$  with  $Q$  being the activation energy in  $\text{kcalmol}^{-1}$  and  $R$  the universal gas constant ( $8.314 \text{ JK}^{-1}\text{mol}^{-1}$ ).

Results from four experimental studies are summarized in Table C.1. Together with the pre-exponential factors and the activation energies, we also evaluate the four different expressions of ice diffusivities for the temperature of  $T = 245\text{K}$ .

When  $D_{\text{ice}}$  is known, a  $\sigma_{\text{ice}}$  calculation can be obtained by solving Eq. 2.5. Using the integrating factor

$F = \exp\left(\int -2\dot{\epsilon}_z(t) dt\right)$  we get:

$$\frac{d}{dt} \left( \sigma_{\text{ice}}^2 e^{\int -2\dot{\epsilon}_z(t) dt} \right) = 2D_{\text{ice}}(t) e^{\int -2\dot{\epsilon}_z(t) dt} \quad (\text{C.2})$$

This finally yields the ice diffusion length for a layer with age  $t'$  that has undergone ice flow thinning  $S(t')$ :

$$\sigma_{ice}^2(t') = S(t')^2 \int_0^{t'} 2D_{ice}(t) S(t)^{-2} dt \quad (C.3)$$

Table C.1: Four experimental studies with their estimated activation energies ( $Q$ ), the pre-exponential factors ( $D_0$ ), the activation energies ( $X$ ), and the corresponding ice diffusivities for the temperature of  $T = 245$  K ( $D_{245}$ ).

	$D_0$ [ $\text{m}^2\text{s}^{-1}$ ]	$Q$ [ $\text{kcalmol}^{-1}$ ]	$X$ [ $\text{K}^{-1}$ ]	$D_{245}$ [ $\text{m}^2\text{s}^{-1}$ ]
Ramseier (1967)	$9.2 \cdot 10^{-4}$	14.28	7186.5	$1.68 \cdot 10^{-16}$
Itagaki (1964)	0.014	14.97	7534.2	$6.18 \cdot 10^{-16}$
Blicks et al. (1966)	$2.5 \cdot 10^{-3}$	14.51	7302.4	$2.85 \cdot 10^{-16}$
Delibaltas et al. (1966)	$2.6 \cdot 10^{-3}$	15.66	7881.9	$2.83 \cdot 10^{-16}$

## APPENDIX D

### GENERATING SYNTHETIC DATA

The time series are generated using an AR-1 process with coefficient  $r_1$  and variance  $\varepsilon$

$$\delta_n - r_1 \delta_{n-1} = \varepsilon_n. \quad (D.1)$$

For the AR-1 process we use  $r_1 = 0.3$  and  $\varepsilon = 120 \text{‰}^2$  for case A and  $200 \text{‰}^2$  for case B. Each data section is 20 m long and has an initial spacing of  $10^{-3}$  m. The  $\delta\text{D}$  and  $\delta^{17}\text{O}$  series are then generated assuming a  $d_{xs}$  signal of  $10 \text{‰}$  and an  $\Delta^{17}\text{O}$  signal of 0 per meg:

$$\delta\text{D} = 8 \cdot \delta^{18}\text{O} + 10 \text{‰} \quad (D.2)$$

$$\Delta^{17}\text{O} = \ln(\delta^{17}\text{O} + 1) - 0.528 \ln(\delta^{18}\text{O} + 1) \quad (D.3)$$

The time series are then forward-diffused by means of numerical convolution with a Gaussian filter of variance  $\sigma_{input}^2$  equal to the diffusion length for every case (Table 4.2). This input diffusion length is calculated as:

$$\sigma_{input}^2 = \sigma^2 \cdot S^2 + \sigma_{ice}^2, \quad (D.4)$$

where  $\sigma^2$  is the firn diffusion. For both case A and B, the ice diffusion is  $\sigma_{ice} = 10^{-3}$  m with a thinning of  $S = 0.80$ . Sampling with a discrete scheme of  $\Delta = 0.025$  m and addition of white measurement noise completes the process of the time series generation. We use a noise level of  $0.05 \text{‰}$ ,  $0.07 \text{‰}$  and  $0.5 \text{‰}$

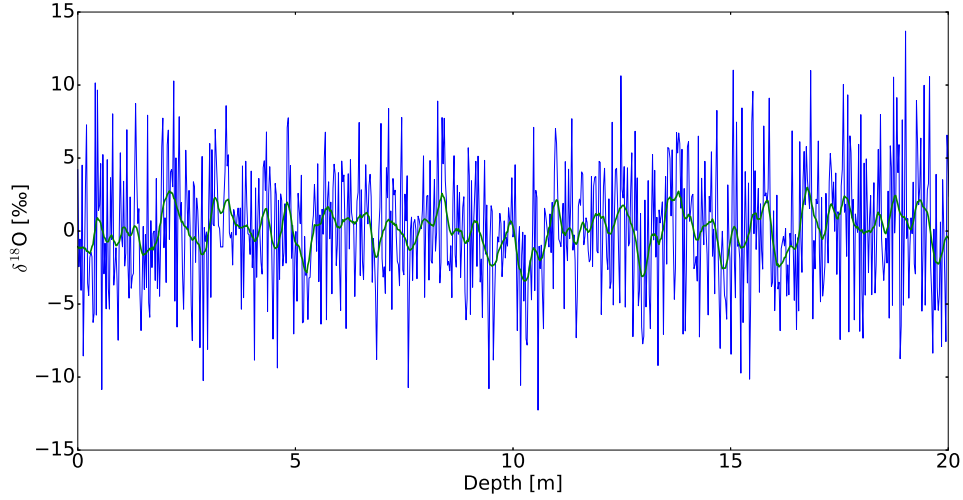


Figure D.1: Synthetic generated  $\delta^{18}\text{O}$  series (case B) which both have been sampled. Blue curve represents the data before diffusion, and the green curve represents the data after diffusion.  $\sigma = 8.4$  cm.

for  $\delta^{17}\text{O}$ ,  $\delta^{18}\text{O}$  and  $\delta\text{D}$  respectively, with the numbers being representative of measurement noise we have been observing over years of ice core measurements in our laboratory.

For a case B scenario, the sampled outputs of the synthetic data before and after diffusion is shown in Fig. D.1. Applying the forward-diffusion smoothens the large amplitudes of the high frequencies. This effect is further illustrated in Fig. D.2 which shows the PSD of the signal before and after diffusion.

## APPENDIX E

### DISCRETE SAMPLING DIFFUSION

The sample diffusion length  $\sigma_{\text{dis}}$  is estimated by setting the transfer function of a Gaussian filter equal to a rectangular filter with width of the sample size  $\Delta$ . The transfer function for the Gaussian filter in Eq. 2.3 is found by its Fourier transform:

$$\mathfrak{F}[\mathcal{G}] = \hat{\mathcal{G}} = e^{-\frac{k^2 \sigma_{\text{dis}}^2}{2}}. \quad (\text{E.1})$$

A regular rectangle function is defined as:

$$\text{rect}(t) = \begin{cases} 1 & \text{for } -\frac{1}{2} < t < \frac{1}{2} \\ \frac{1}{2} & \text{for } t = \left|\frac{1}{2}\right| \\ 0 & \text{for } t > \left|\frac{1}{2}\right| \end{cases} \quad (\text{E.2})$$

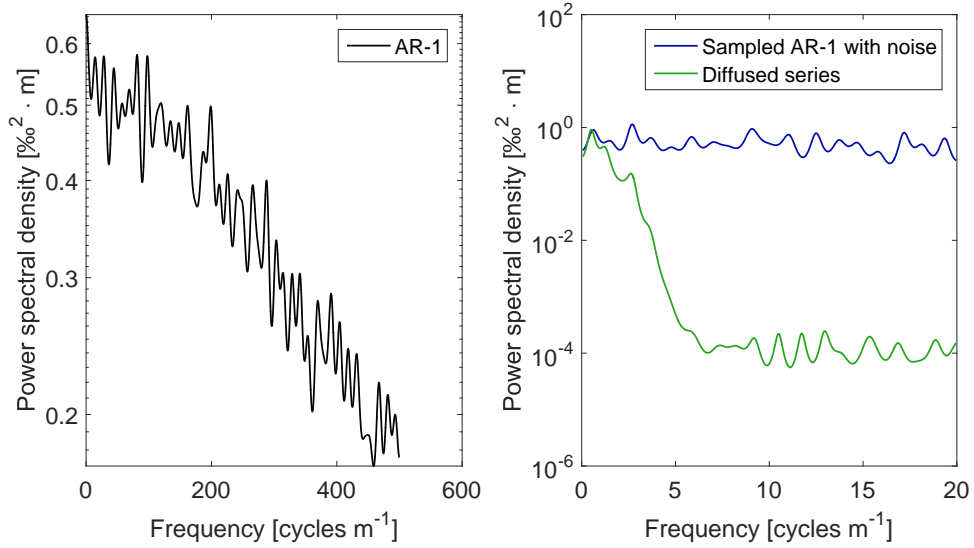


Figure D.2: Left: PSD of the raw AR-1 time series (case B  $\delta^{18}\text{O}$  series). Right: PSD of the  $\delta^{18}\text{O}$  series (from Fig. D.1). Blue curve represents the PSD of the sampled time series before diffusion, and the green curve represents the PSD of the sampled time series after diffusion. The y-scale are different in the two figures.

716 This can be transformed into a rectangular function ( $\Pi(t)$ ) with width  $\Delta$  and amplitude  $A$ :

$$\Pi(t) = A \cdot \text{rect}(t \cdot \Delta), \quad \text{for } -\frac{\Delta}{2} < t < \frac{\Delta}{2}. \quad (\text{E.3})$$

717 Normalization yields an amplitude of  $A = 1/\Delta$ . The Fourier transformation of the rectangular pulse is  
718 written as:

$$\hat{\Pi}(f) = \int_{-\infty}^{\infty} \Pi(t) e^{-2\pi i f t} dt = \int_{-\Delta/2}^{\Delta/2} \frac{1}{\Delta} e^{-2\pi i f_{\text{Nq}} t} dt, \quad (\text{E.4})$$

719 where  $f_{\text{Nq}} = 1/(2\Delta)$  is the Nyquist frequency. Setting equations E.1 and E.4 equal to each other:

$$e^{-\frac{k^2 \sigma_{\text{dis}}^2}{2}} = \int_{-\Delta/2}^{\Delta/2} \frac{1}{\Delta} e^{-2\pi i f_{\text{Nq}} t} dt, \quad (\text{E.5})$$

720 where  $k = 2\pi f_{\text{Nq}}$ . This results in the following solution for the discrete sampling diffusion length:

$$\sigma_{\text{dis}}^2 = \frac{2\Delta^2}{\pi^2} \ln\left(\frac{\pi}{2}\right). \quad (\text{E.6})$$

## APPENDIX F

## FIGURES

Here we provide figures that show the performance of each diffusion technique. For each data section we have the estimated uncorrected diffusion lengths in a table.

### F.1 NEEM - late Holocene

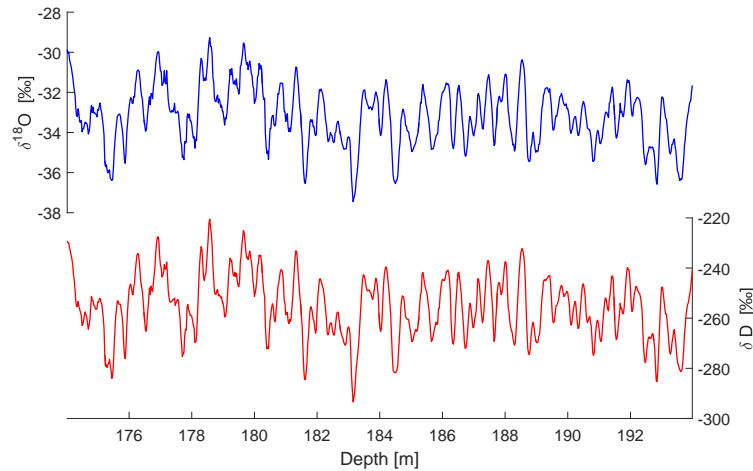


Figure F.1: NEEM. Late Holocene  $\delta^{18}\text{O}$  (top) and  $\delta\text{D}$  (below) profiles with depth.

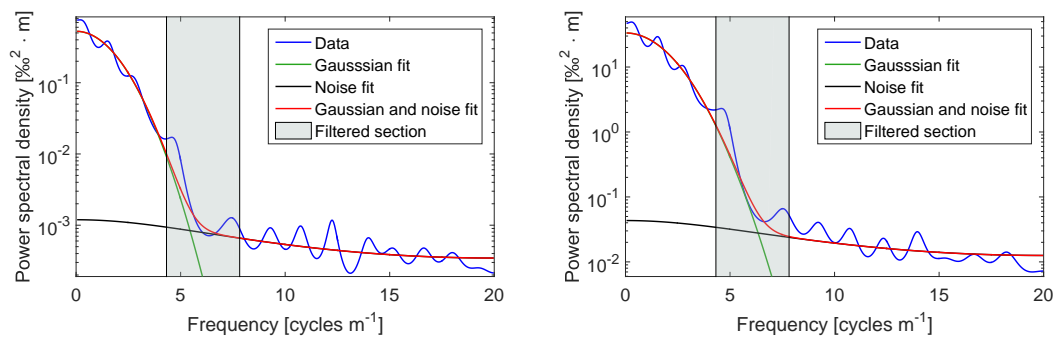


Figure F.2: NEEM. Late Holocene power spectra of  $\delta^{18}\text{O}$  (left) and  $\delta\text{D}$  (right).

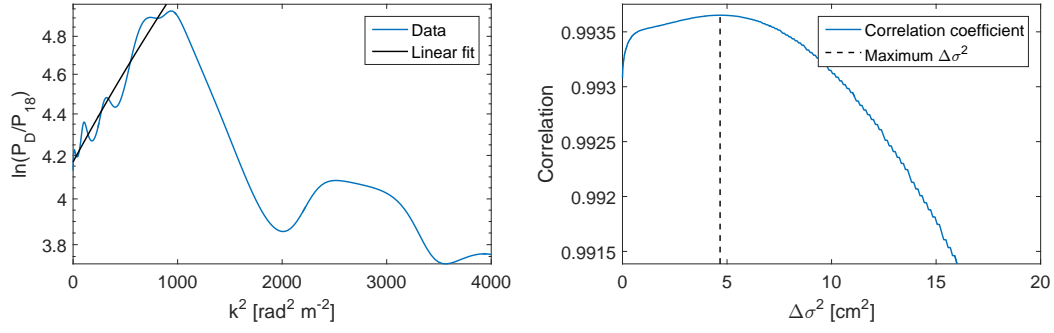


Figure F.3: Differential diffusion techniques applied on NEEM late Holocene data. Left: linear fit of the logarithmic PSD ratio ( $^{18}\Delta\sigma^2$  II). Right: Correlation between  $\delta^{18}\text{O}$  and artificially diffused  $\delta\text{D}$  ( $^{18}\Delta\sigma^2$  III).

Table F.1: Estimated diffusion values for the NEEM late Holocene data. The values have not been corrected for sampling diffusion, ice diffusion and thinning.

$\sigma_{18}$ [cm]	$\sigma_D$ [cm]	$\Delta\sigma^2$ I [cm²]	$\Delta\sigma^2$ [cm²] II	$\Delta\sigma^2$ III [cm²]
7.41	6.68	10.3	9.0	4.7



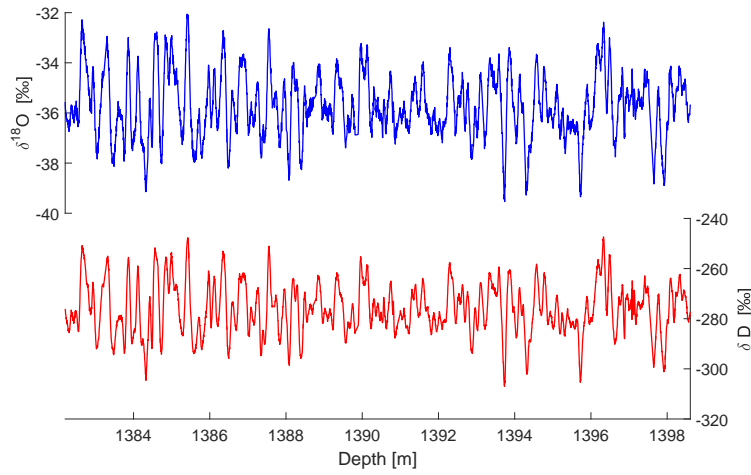
726 *F.2 NEEM - CFA data section*

Figure F.4: NEEM - CFA data. Early Holocene  $\delta^{18}\text{O}$  (top) and  $\delta\text{D}$  (below) profiles with depth.

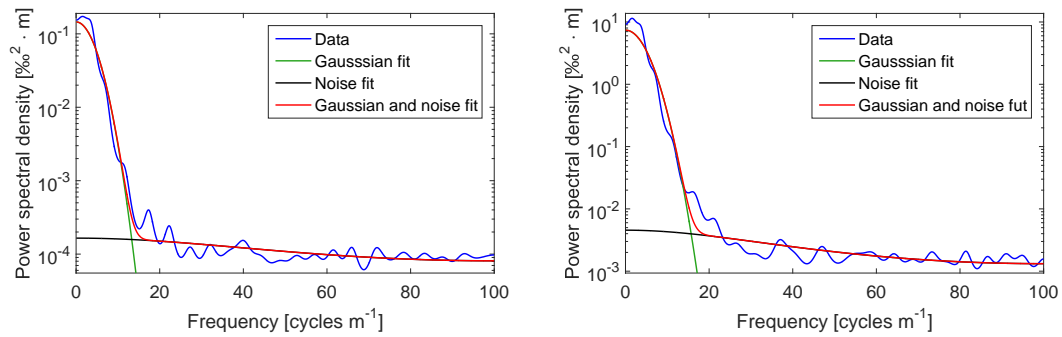


Figure F.5: NEEM - CFA data. Early Holocene power spectra of  $\delta^{18}\text{O}$  (left) and  $\delta\text{D}$  (right)

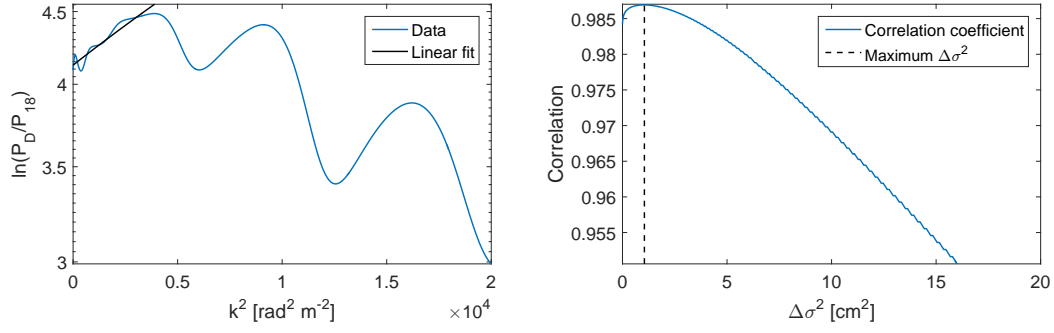


Figure F.6: Differential diffusion techniques applied on NEEM early Holocene CFA data. Left: linear fit of the logarithmic PSD ratio ( $^{18}\Delta\sigma^2$  II). Right: Correlation between  $\delta^{18}\text{O}$  and artificially diffused  $\delta\text{D}$  ( $^{18}\Delta\sigma^2$  III).

Table F.2: Estimated values for NEEM early Holocene CFA data. The values have not been corrected for sampling diffusion, ice diffusion and thinning.

$\sigma_{18}$ [cm]	$\sigma_D$ [cm]	$\Delta\sigma^2$ I [ $\text{cm}^2$ ]	$\Delta\sigma^2$ [ $\text{cm}^2$ ] II	$\Delta\sigma^2$ III [ $\text{cm}^2$ ]
3.12	2.78	2.0	1.1	1.0

727 *F.3 NEEM - discrete data section*

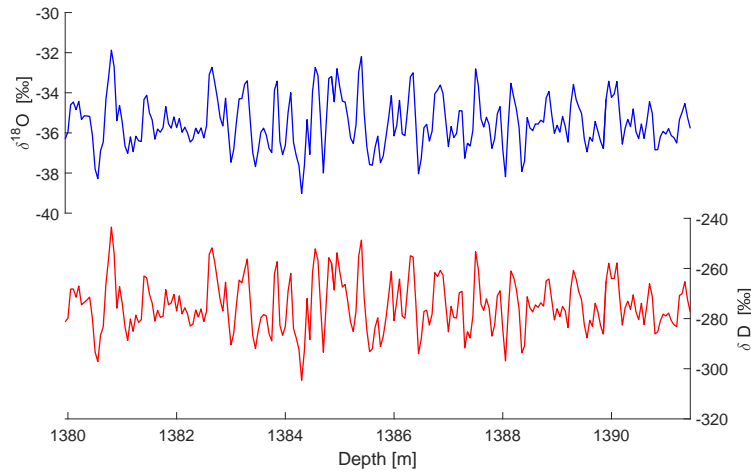


Figure F.7: NEEM - discrete data. Early Holocene  $\delta^{18}\text{O}$  (top) and  $\delta\text{D}$  (below) profiles with depth.

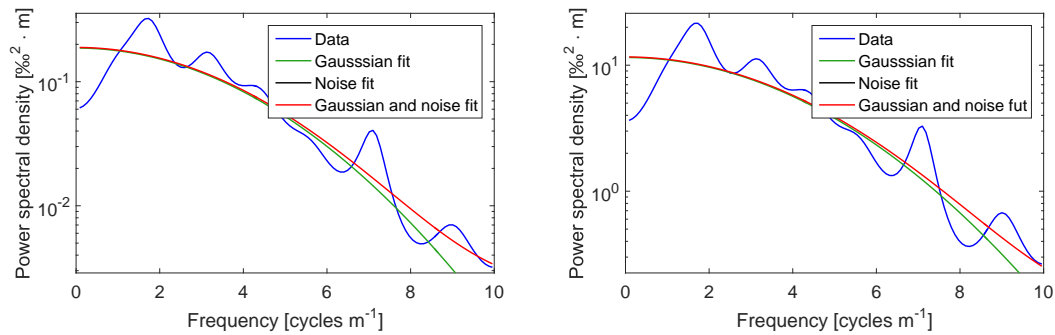


Figure F.8: NEEM - discrete data. Early Holocene power spectra of  $\delta^{18}\text{O}$  (left) and  $\delta\text{D}$  (right)

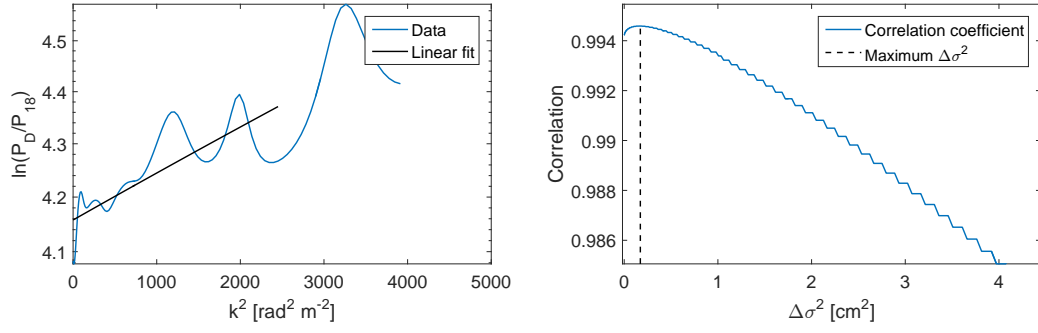


Figure F.9: Differential diffusion techniques applied on NEEM early Holocene discrete data. Left: linear fit of the logarithmic PSD ratio ( $^{18}\Delta\sigma^2$  II). Right: Correlation between  $\delta^{18}\text{O}$  and artificially diffused  $\delta\text{D}$  ( $^{18}\Delta\sigma^2$  III).

Table F.3: Estimated values for NEEM early Holocene discrete data. The values have not been corrected for sampling diffusion, ice diffusion and thinning.

$\sigma_{18}$ [cm]	$\sigma_D$ [cm]	$\Delta\sigma^2$ I [cm <sup>2</sup> ]	$\Delta\sigma^2$ [cm <sup>2</sup> ] II	$\Delta\sigma^2$ III [cm <sup>2</sup> ]
3.58	3.35	1.6	0.9	0.2

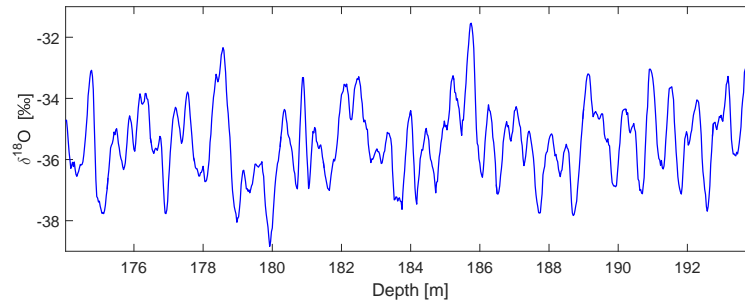
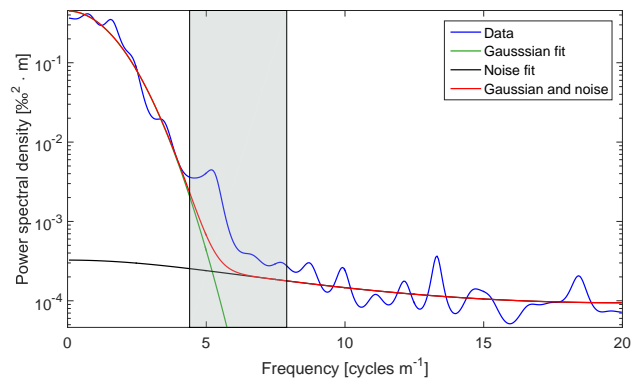
728 *F.4 NGRIP - late Holocene*Figure F.10: NGRIP late Holocene  $\delta^{18}\text{O}$  (top) and  $\delta\text{D}$  (below) profiles with depth.Figure F.11: NGRIP late Holocene power spectrum of  $\delta^{18}\text{O}$ .

Table F.4: Estimated value for NGRIP late Holocene data. The value has not been corrected for sampling diffusion, ice diffusion and thinning.

$\sigma_{18}$ [cm]	$\sigma_{\text{D}}$ [cm]	$\Delta\sigma^2$ I [cm <sup>2</sup> ]	$\Delta\sigma^2$ [cm <sup>2</sup> ] II	$\Delta\sigma^2$ III [cm <sup>2</sup> ]
8.39	-	-	-	-

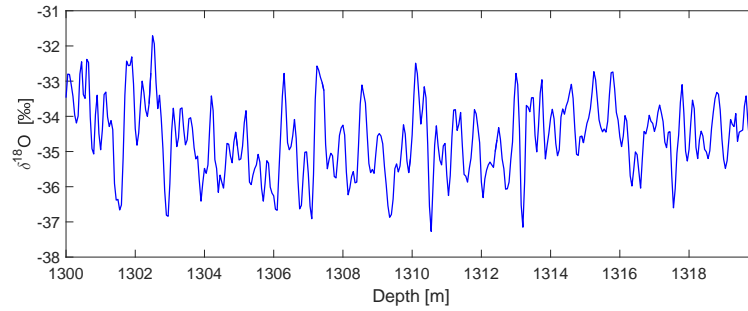
729 *F.5 NGRIP - early Holocene core 1*

Figure F.12: NGRIP early Holocene core 1.  $\delta^{18}\text{O}$  (top) and  $\delta\text{D}$  (below) profiles with depth.

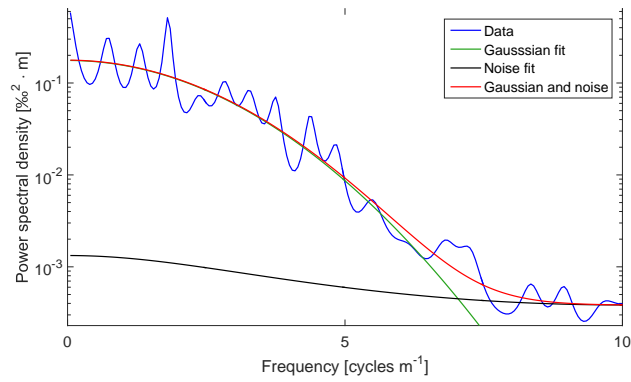


Figure F.13: NGRIP early Holocene core 1. Power spectrum of  $\delta^{18}\text{O}$ .

Table F.5: Estimated value for NGRIP early Holocene core 1 data. The value has not been corrected for sampling diffusion, ice diffusion and thinning.

$\sigma_{18}$ [cm]	$\sigma_{\text{D}}$ [cm]	$\Delta\sigma^2$ I [cm <sup>2</sup> ]	$\Delta\sigma^2$ [cm <sup>2</sup> ] II	$\Delta\sigma^2$ III [cm <sup>2</sup> ]
5.53	-	-	-	-

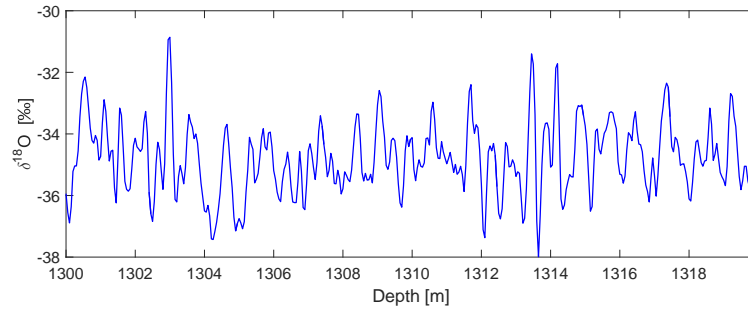
730 *F.6 NGRIP - early Holocene core 2*

Figure F.14: NGRIP early Holocene core 2.  $\delta^{18}\text{O}$  (top) and  $\delta\text{D}$  (below) profiles with depth.

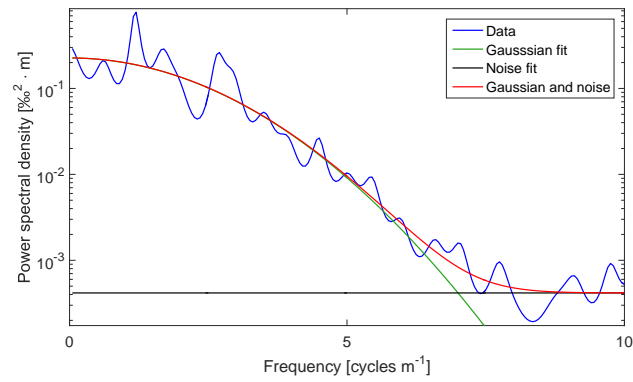


Figure F.15: NGRIP early Holocene core 2. Power spectrum of  $\delta^{18}\text{O}$ .

Table F.6: Estimated value for NGRIP early Holocene core 2 data. The value has not been corrected for sampling diffusion, ice diffusion and thinning.

$\sigma_{18}$ [cm]	$\sigma_{\text{D}}$ [cm]	$\Delta\sigma^2$ I [cm <sup>2</sup> ]	$\Delta\sigma^2$ [cm <sup>2</sup> ] II	$\Delta\sigma^2$ III [cm <sup>2</sup> ]
5.70	-	-	-	-

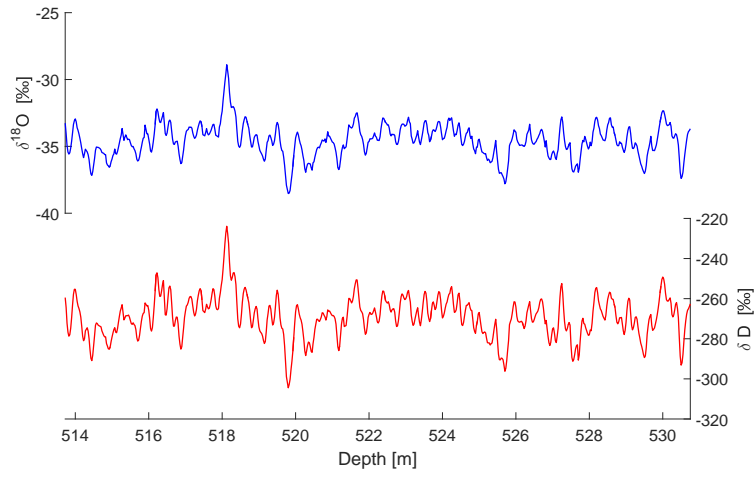
731 *F.7 GRIP - late Holocene*

Figure F.16: GRIP. Late Holocene  $\delta^{18}\text{O}$  (top) and  $\delta\text{D}$  (below) profiles with depth.

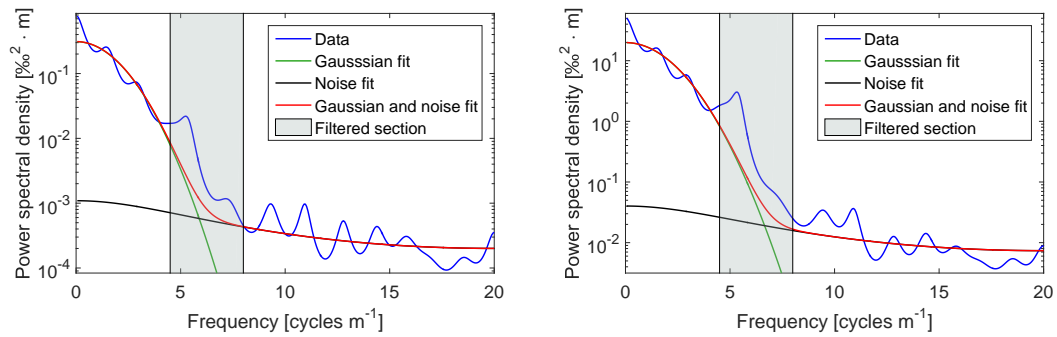


Figure F.17: GRIP. Late Holocene power spectra of  $\delta^{18}\text{O}$  (left) and  $\delta\text{D}$  (right).



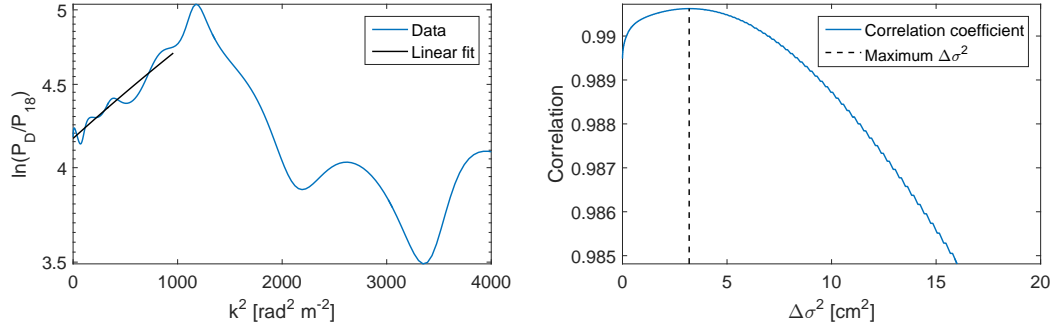


Figure F.18: Differential diffusion techniques applied on GRIP late Holocene data. Left: linear fit of the logarithmic PSD ratio ( $^{18}\Delta\sigma^2$  II). Right: Correlation between  $\delta^{18}\text{O}$  and artificially diffused  $\delta\text{D}$  ( $^{18}\Delta\sigma^2$  III).

Table F.7: Estimated diffusion values for the GRIP late Holocene data. The values have not been corrected for sampling diffusion, ice diffusion and thinning.

$\sigma_{18}$ [cm]	$\sigma_D$ [cm]	$\Delta\sigma^2$ I [ $\text{cm}^2$ ]	$\Delta\sigma^2$ [ $\text{cm}^2$ ] II	$\Delta\sigma^2$ III [ $\text{cm}^2$ ]
6.78	6.31	6.2	5.6	3.2

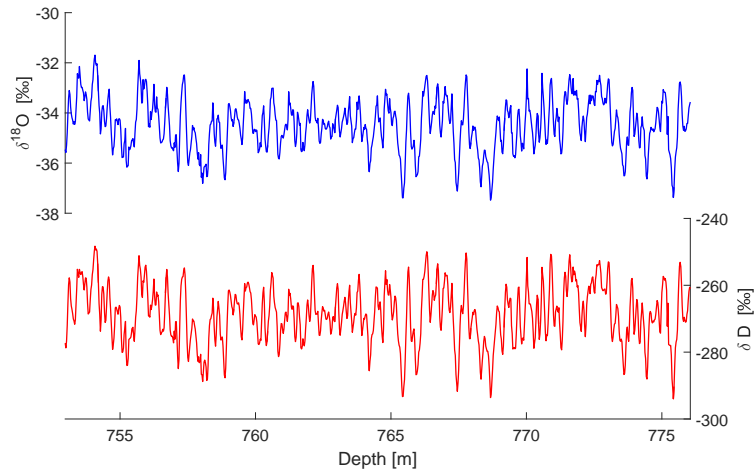
732 *F.8 GRIP - mid Holocene*

Figure F.19: GRIP. Mid Holocene  $\delta^{18}\text{O}$  (top) and  $\delta\text{D}$  (below) profiles with depth.

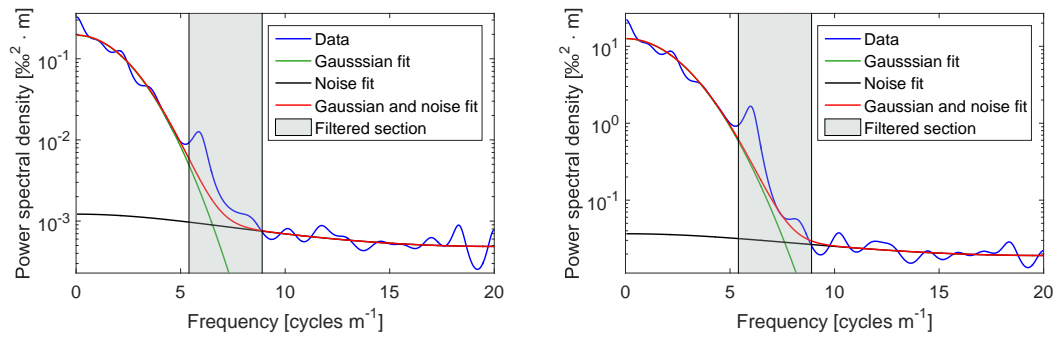


Figure F.20: GRIP. Mid Holocene power spectra of  $\delta^{18}\text{O}$  (left) and  $\delta\text{D}$  (right).

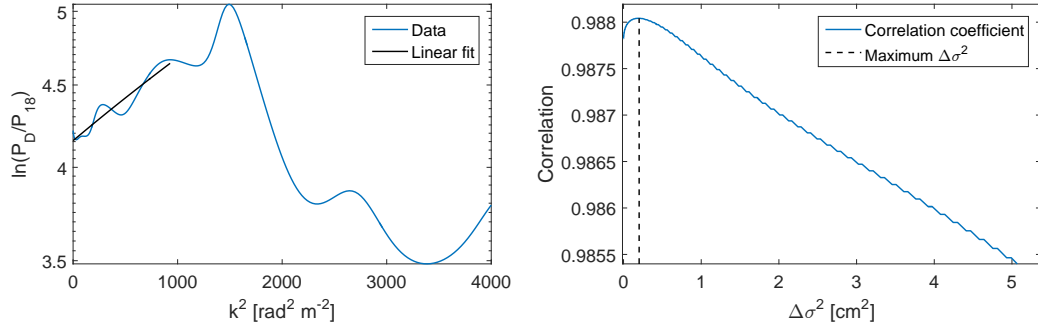


Figure F.21: Differential diffusion techniques applied on GRIP mid Holocene data. Left: linear fit of the logarithmic PSD ratio ( $^{18}\Delta\sigma^2$  II). Right: Correlation between  $\delta^{18}\text{O}$  and artificially diffused  $\delta D$  ( $^{18}\Delta\sigma^2$  III).

Table F.8: Estimated diffusion values for the GRIP mid Holocene data. The values have not been corrected for sampling diffusion, ice diffusion and thinning.

$\sigma_{18}$ [cm]	$\sigma_D$ [cm]	$\Delta\sigma^2$ I [cm <sup>2</sup> ]	$\Delta\sigma^2$ [cm <sup>2</sup> ] II	$\Delta\sigma^2$ III [cm <sup>2</sup> ]
5.66	5.16	5.3	5.2	0.2

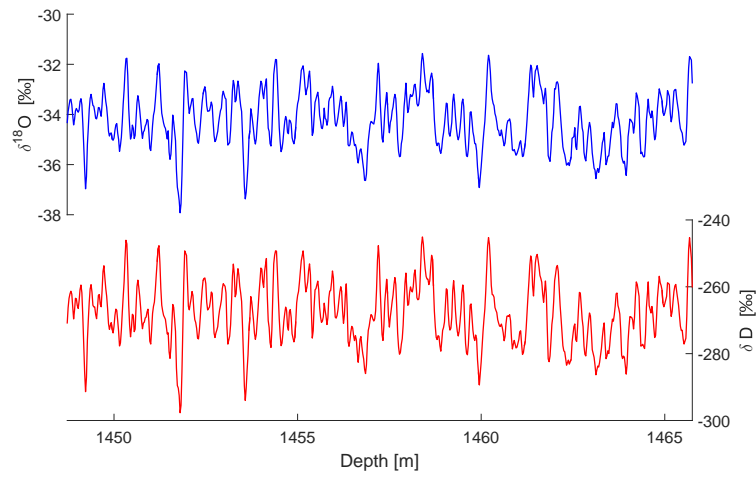


Figure F.22: GRIP. Early Holocene  $\delta^{18}\text{O}$  (top) and  $\delta\text{D}$  (below) profiles with depth.

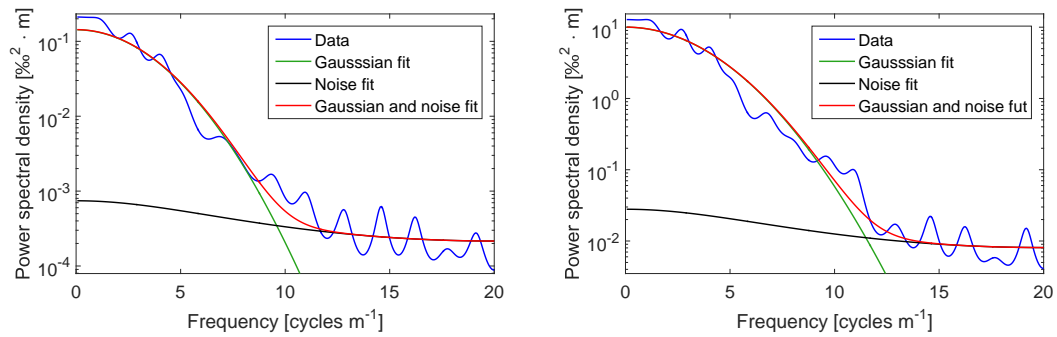


Figure F.23: GRIP. Early Holocene power spectra of  $\delta^{18}\text{O}$  (left) and  $\delta\text{D}$  (right).

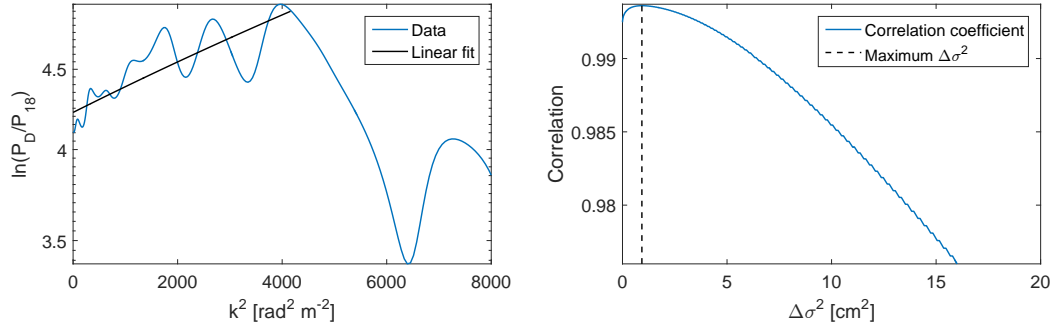


Figure F.24: Differential diffusion techniques applied on GRIP early Holocene data. Left: linear fit of the logarithmic PSD ratio ( $^{18}\Delta\sigma^2$  II). Right: Correlation between  $\delta^{18}\text{O}$  and artificially diffused  $\delta\text{D}$  ( $^{18}\Delta\sigma^2$  III).

Table F.9: Estimated diffusion values for the GRIP early Holocene data. The values have not been corrected for sampling diffusion, ice diffusion and thinning.

$\sigma_{18}$ [cm]	$\sigma_D$ [cm]	$\Delta\sigma^2$ I [ $\text{cm}^2$ ]	$\Delta\sigma^2$ [ $\text{cm}^2$ ] II	$\Delta\sigma^2$ III [ $\text{cm}^2$ ]
4.07	3.61	3.5	1.6	0.9

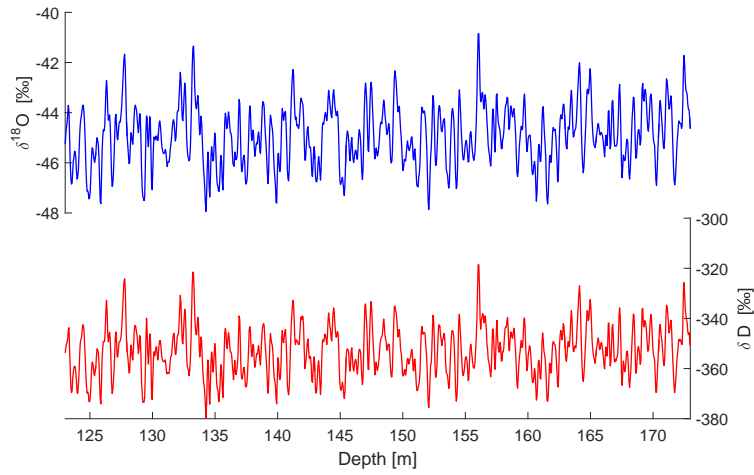


Figure F.25: EDML.  $\delta^{18}\text{O}$  (top) and  $\delta\text{D}$  (below) profiles with depth.

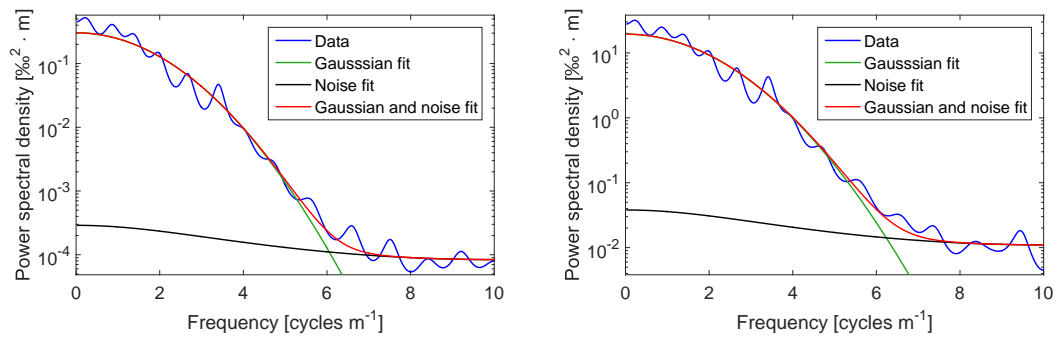


Figure F.26: EDML. Power spectra of  $\delta^{18}\text{O}$  (left) and  $\delta\text{D}$  (right).

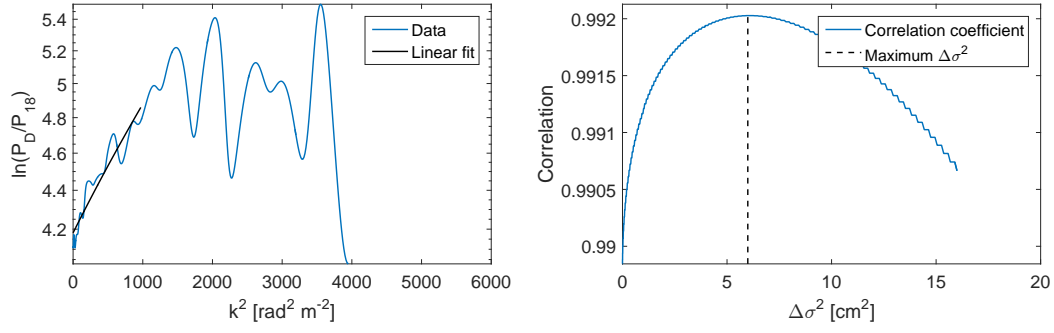


Figure F.27: Differential diffusion techniques applied on EDML Holocene data. Left: linear fit of the logarithmic PSD ratio ( $^{18}\Delta\sigma^2$  II). Right: Correlation between  $\delta^{18}\text{O}$  and artificially diffused  $\delta\text{D}$  ( $^{18}\Delta\sigma^2$  III).

Table F.10: Estimated diffusion values for the EDML data. The values have not been corrected for sampling diffusion, ice diffusion and thinning.

$\sigma_{18}$ [cm]	$\sigma_D$ [cm]	$\Delta\sigma^2$ I [cm <sup>2</sup> ]	$\Delta\sigma^2$ [cm <sup>2</sup> ] II	$\Delta\sigma^2$ III [cm <sup>2</sup> ]
7.40	6.86	7.7	7.0	6.0

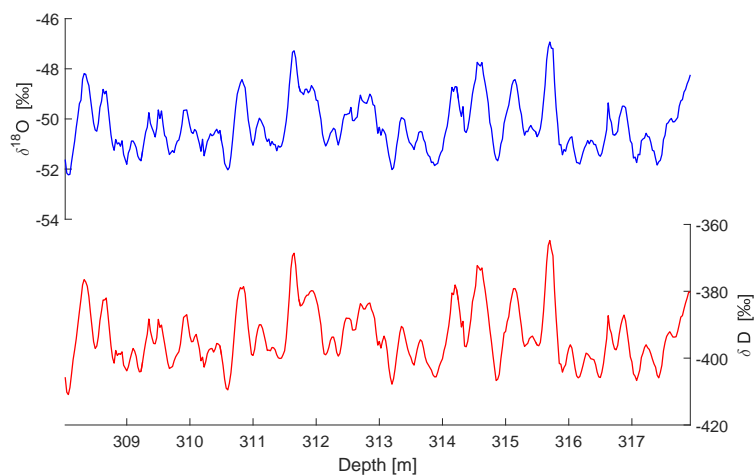


Figure F.28: Dome C.  $\delta^{18}\text{O}$  (top) and  $\delta\text{D}$  (below) profiles with depth.

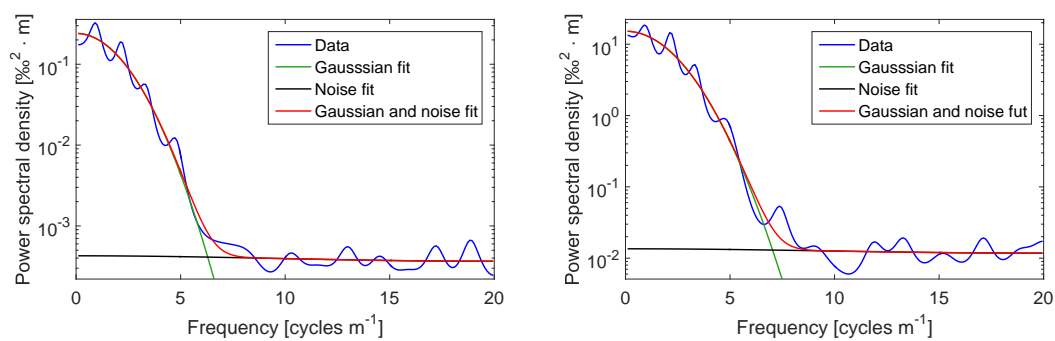


Figure F.29: Dome C. Power spectra of  $\delta^{18}\text{O}$  (left) and  $\delta\text{D}$  (right).



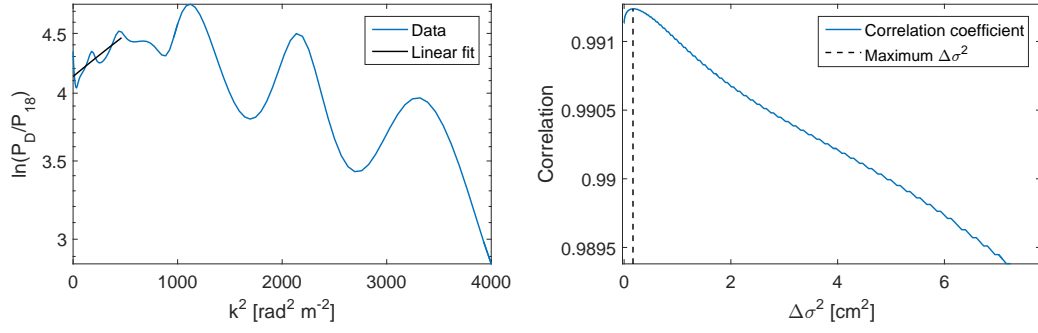


Figure F.30: Differential diffusion techniques applied on Dome C Holocene data. Left: linear fit of the logarithmic PSD ratio ( $^{18}\Delta\sigma^2$  II). Right: Correlation between  $\delta^{18}\text{O}$  and artificially diffused  $\delta\text{D}$  ( $^{18}\Delta\sigma^2$  III).

Table F.11: Estimated diffusion values for the Dome C data. The values have not been corrected for sampling diffusion, ice diffusion and thinning.

$\sigma_{18}$ [cm]	$\sigma_D$ [cm]	$\Delta\sigma^2$ I [cm <sup>2</sup> ]	$\Delta\sigma^2$ [cm <sup>2</sup> ] II	$\Delta\sigma^2$ III [cm <sup>2</sup> ]
6.38	6.01	4.6	7.1	0.2

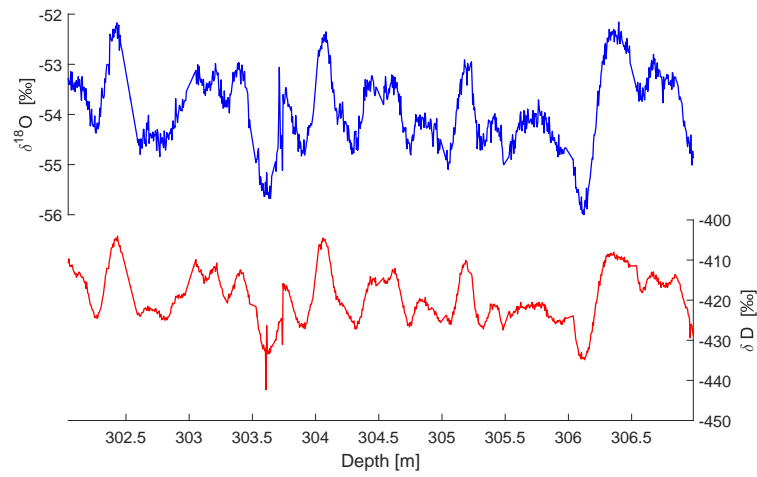


Figure F.31: Dome F.  $\delta^{18}\text{O}$  (top) and  $\delta\text{D}$  (below) profiles with depth.

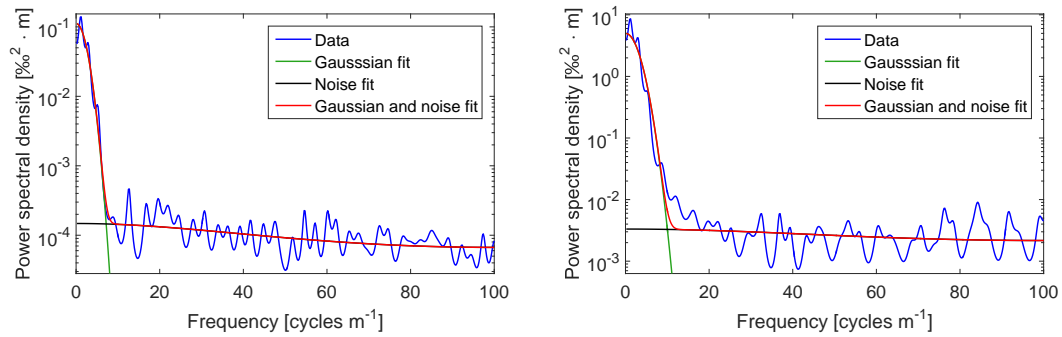


Figure F.32: Dome F. Power spectra of  $\delta^{18}\text{O}$  (left) and  $\delta\text{D}$  (right).

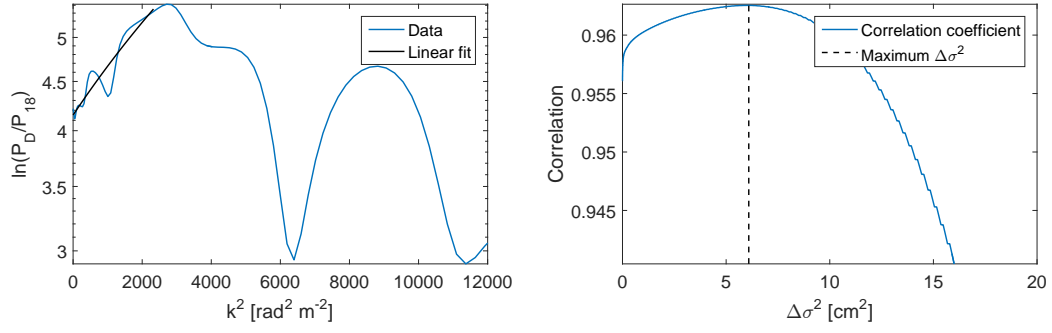


Figure F.33: Differential diffusion techniques applied on Dome F Holocene data. Left: linear fit of the logarithmic PSD ratio ( $^{18}\Delta\sigma^2$  II). Right: Correlation between  $\delta^{18}\text{O}$  and artificially diffused  $\delta\text{D}$  ( $^{18}\Delta\sigma^2$  III).

Table F.12: Estimated diffusion values for the Dome F data. The values have not been corrected for sampling diffusion, ice diffusion and thinning.

$\sigma_{18}$ [cm]	$\sigma_D$ [cm]	$\Delta\sigma^2$ I [ $\text{cm}^2$ ]	$\Delta\sigma^2$ [ $\text{cm}^2$ ] II	$\Delta\sigma^2$ III [ $\text{cm}^2$ ]
5.70	4.30	14.0	5.2	6.1

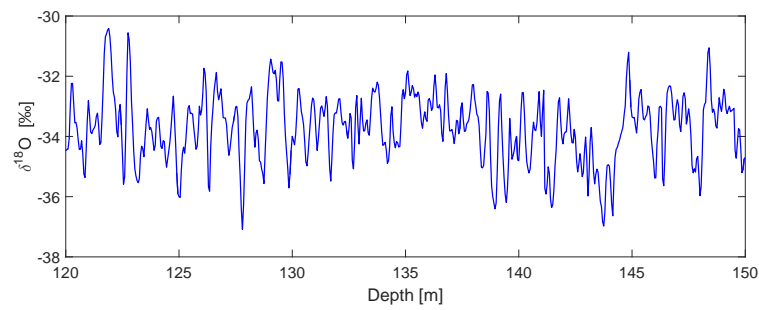


Figure F.34: WAIS D.  $\delta^{18}\text{O}$  (top) and  $\delta\text{D}$  (below) profiles with depth.

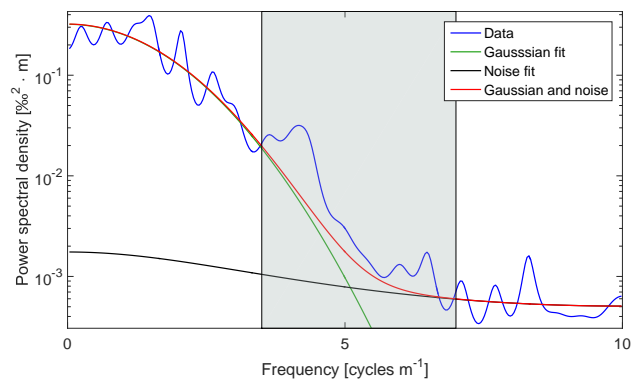


Figure F.35: WAIS D. Holocene power spectra of  $\delta^{18}\text{O}$ .

Table F.13: Estimated value for WAIS D Holocene data. The value has not been corrected for sampling diffusion, ice diffusion and thinning.

$\sigma_{18}$ [cm]	$\sigma_{\text{D}}$ [cm]	$\Delta\sigma^2$ I [cm <sup>2</sup> ]	$\Delta\sigma^2$ [cm <sup>2</sup> ] II	$\Delta\sigma^2$ III [cm <sup>2</sup> ]
7.23	-	-	-	-

REFERENCES

739 Abramowitz, M. & Stegun, I. A. (1964), *Handbook of Mathematical Functions with Formulas, Graphs,*  
740 *and Mathematical Tables*, 9th edn, Dover.

- Adolph, A. C. & Albert, M. R. (2014), 'Gas diffusivity and permeability through the firn column at Summit, Greenland: measurements and comparison to microstructural properties', *The Cryosphere* **8**, 319–328.
- Andersen, N. (1974), 'On The Calculation Of Filter Coefficients For Maximum Entropy Spectral Analysis', *Geophysics* **39**(1).
- Baker, L., Franchi, I. A., Maynard, J., Wright, I. P. & Pillinger, C. T. (2002), 'A technique for the determination of O-18/O-16 and O-17/O-16 isotopic ratios in water from small liquid and solid samples', *Analytical Chemistry* **74**(7), 1665–1673.
- Banta, J. R., McConnell, J. R., Frey, M. M., Bales, R. C. & Taylor, K. (2008), 'Spatial and temporal variability in snow accumulation at the West Antarctic Ice Sheet Divide over recent centuries', *Journal of Geophysical Research* **113**.
- Barkan, E. & Luz, B. (2005), 'High precision measurements of O-17/O-16 and O-18/O-16 ratios in (H<sub>2</sub>O)', *Rapid Communications In Mass Spectrometry* **19**(24), 3737–3742.
- Barkan, E. & Luz, B. (2007), 'Diffusivity fractionations of (H<sub>2</sub>O)-O-16/(H<sub>2</sub>O)-O-17 and (H<sub>2</sub>O)-O-16/(H<sub>2</sub>O)-O-18 in air and their implications for isotope hydrology', *Rapid Communications In Mass Spectrometry* **21**(18), 2999–3005.
- Begley, I. S. & Scrimgeour, C. M. (1997), 'High-precision  $\delta^2\text{H}$  and  $\delta^{18}\text{O}$  measurement for water and volatile organic compounds by continuous-flow pyrolysis isotope ratio mass spectrometry', *Analytical Chemistry* **69**(8), 1530–1535.
- Bigeleisen, J., Perlman, M. L. & Prosser, H. C. (1952), 'Conversion of hydrogenic materials to hydrogen for isotopic analysis', *Analytical Chemistry* **24**(8), 1356–1357.
- Blicks, H., Dengel, O. & Riehl, N. (1966), 'Diffusion von protonen (tritonen) in reinen und dotierten eis-einkristallen', *Physik Der Kondensierten Materie* **4**(5), 375–381.
- Brand, W. A., Geilmann, H., Crosson, E. R. & Rella, C. W. (2009), 'Cavity ring-down spectroscopy versus high-temperature conversion isotope ratio mass spectrometry; a case study on  $\delta^2\text{H}$  and  $\delta^{18}\text{O}$  of pure water samples and alcohol/water mixtures', *Rapid Communications in Mass Spectrometry* **23**(12), 1879–1884.
- Craig, H. (1961), 'Isotopic Variations in Meteoric Water', *Science* **133**(3465), 1702–1703.
- Crosson, E. R. (2008), 'A cavity ring-down analyzer for measuring atmospheric levels of methane, carbon dioxide, and water vapor', *Applied Physics B-Lasers And Optics* **92**(3), 403–408.
- Cuffey, K. M., Alley, R. B., Grootes, P. M., Bolzan, J. M. & Anandakrishnan, S. (1994), 'Calibration Of the Delta-O-18 isotopic paleothermometer for central Greenland, using borehole temperatures', *Journal Of Glaciology* **40**(135), 341–349.

- Cuffey, K. M. & Paterson, W. S. B. (2010), *The physics of glaciers*, 4th edn, Elsevier.
- Dahl-Jensen, D., Mosegaard, K., Gundestrup, N., Clow, G. D., Johnsen, S. J., Hansen, A. W. & Balling, N. (1998), 'Past temperatures directly from the Greenland Ice Sheet', *Science* **282**(5387), 268–271.
- Dansgaard, W. (1954), 'The  $^{18}\text{O}$ -abundance in fresh water', *Geochimica et Cosmochimica Acta* **6**(5–6), 241–260.
- Dansgaard, W. (1964), 'Stable isotopes in precipitation', *Tellus B* **16**(4), 436–468.
- Dansgaard, W. & Johnsen, S. J. (1969), 'A flow model and a time scale for the ice core from Camp Century, Greenland', *Journal of Glaciology* **8**(53).
- Delibaltas, P., Dengel, O., Helmreich, D., Riehl, N. & Simon, H. (1966), 'Diffusion von  $^{18}\text{O}$  in einkristallen', *Physik Der Kondensierten Materie* **5**(3), 166–170.
- Durran, D. R. (2010), *Numerical Methods for Fluid Dynamics*, Springer, 2nd. Edition.
- Ellehoj, M. D., Steen-Larsen, H. C., Johnsen, S. J. & Madsen, M. B. (2013), 'Ice-vapor equilibrium fractionation factor of hydrogen and oxygen isotopes: Experimental investigations and implications for stable water isotope studies', *Rapid Communications in Mass Spectrometry* **27**, 2149–2158.
- Emanuelsson, B. D., Baisden, W. T., Bertler, N. A. N., Keller, E. D. & Gkinis, V. (2015), 'High-resolution continuous-flow analysis setup for water isotopic measurement from ice cores using laser spectroscopy', *Atmos. Meas. Tech.* **8**(7), 2869–2883.
- Epstein, S., Buchsbaum, R., Lowenstam, H. & Urey, H. (1951), 'Carbonate-water isotopic temperature scale', *Geological Society of America Bulletin* **62**(4), 417.
- Freitag, J., Dorbrindt, U. & Kipfstuhl, S. (2002), 'A new method for predicting transport properties of polar firn with respect to gases on the pore space scale', *Ann. Glacio.* **35**, 538–544.
- Gehre, M., Hoefling, R., Kowski, P. & Strauch, G. (1996), 'Sample preparation device for quantitative hydrogen isotope analysis using chromium metal', *Analytical Chemistry* **68**(24), 4414–4417.
- Gkinis, V. (2011), High resolution water isotope data from ice cores, PhD thesis, University of Copenhagen.
- Gkinis, V., Popp, T. J., Blunier, T., Bigler, M., Schupbach, S., Kettner, E. & Johnsen, S. J. (2011), 'Water isotopic ratios from a continuously melted ice core sample', *Atmospheric Measurement Techniques* **4**(11), 2531–2542.
- Gkinis, V., Simonsen, S. B., Buchardt, S. L., White, J. W. C. & Vinther, B. M. (2014), 'Water isotope diffusion rates from the NorthGRIP ice core for the last 16,000 years - glaciological and paleoclimatic implications', *Earth and Planetary Science Letters* **405**.
- Guillevic, M., Bazin, L., Landais, A., Kindler, P., Orsi, A., Masson-Delmotte, V., Blunier, T., Buchardt, S. L., Capron, E., Leuenberger, M. ., Martinerie, P., Prie, F. & Vinther, B. M. (2013), 'Spatial gradients

of temperature, accumulation and  $\delta^{18}\text{O}$ -ice in Greenland over a series of Dansgaard-Oeschger events', *Climate of the Past* **9**, 1029–1051.

Hall, W. D. & Pruppacher, H. R. (1976), 'The Survival of Ice Particles Falling from Cirrus Clouds in Subsaturated Air', *Journal of the Atmospheric Sciences* **33**(10), 1995–2006.

Itagaki, K. (1964), 'Self-diffusion in single crystals of ice', *J. Phys. Soc. Jpn.* **19**(6), 1081–1081.

Johnsen, S., Clausen, H. B., Cuffey, K. M., Hoffmann, G., Schwander, J. & Creyts, T. (2000), 'Diffusion of stable isotopes in polar firn and ice: the isotope effect in firn diffusion', *Physics of Ice Core Records* pp. 121–140.

Johnsen, S. J. (1977), 'Stable Isotope Homogenization of Polar Firn and Ice', *Isotopes and Impurities in Snow and Ice* pp. 210–219.

Johnsen, S. J., Dahl Jensen, D., Dansgaard, W. & Gundestrup, N. (1995), 'Greenland paleotemperatures derived from GRIP bore hole temperature and ice core isotope profiles', *Tellus B-Chemical And Physical Meteorology* **47**(5), 624–629.

Johnsen, S. J., Dahl-Jensen, D., Gundestrup, N., Steffensen, J. P., Clausen, H. B., Miller, H., Masson-Delmotte, V., Sveinbjrnsdottir, A. E. & White, J. (2001), 'Oxygen isotope and palaeotemperature records from six Greenland ice-core stations: Camp Century, Dye-3, GRIP, GISP2, Renland and NorthGRIP', *Journal of Quaternary Science* **16**(4).

Johnsen, S. J. & White, J. (1989), 'The origin of Arctic precipitation under present and glacial conditions', *Tellus* **41B**, 452–468.

Jones, T. R., White, J. W. C., Steig, E. J., Vaughn, B. H., Morris, V., Gkinis, V., Markle, B. R. & Schoenemann, S. W. (2017), 'Improved methodologies for continuous-flow analysis of stable water isotopes in ice cores', *Atmos. Meas. Tech* **10**, 617–632.

Jouzel, J., Alley, R. B., Cuffey, K. M., Dansgaard, W., Grootes, P., Hoffmann, G., Johnsen, S. J., Koster, R. D., Peel, D., Shuman, C. A., Stievenard, M., Stuiver, M. & White, J. (1997), 'Validity of the temperature reconstruction from water isotopes in ice cores', *Journal Of Geophysical Research-Oceans* **102**(C12), 26471–26487.

Jouzel, J. & Merlivat, L. (1984), 'Deuterium and oxygen 18 in precipitation: modeling of the isotopic effects during snow formation', *Journal of Geophysical Research-Atmospheres* **89**(D7), 11749 – 11759.

Kawamura, K., Nakazawa, T., Aoki, S., Sugawara, S., Fujii, Y. & Watanabe, O. (2003), 'Atmospheric CO<sub>2</sub> variations over the last three glacial-interglacial climatic cycles deduced from the Dome Fuji deep ice core, Antarctica using a wet extraction technique', *Tellus* **55B**, 126–137.

Kay, S. M. & Marple, S. L. (1981), 'Spectrum Analysis - A Modern Perspective', *Proceedings of the IEEE* **69**(11).

- Lamb, K. D., Clouser, B. W., Bolot, M., Sarkozy, L., Ebert, V., Saathoff, H., Möhler, O. & Moyer, E. J. (2017), ‘Laboratory measurements of HDO/H<sub>2</sub>O isotopic fractionation during ice deposition in simulated cirrus clouds’.
- Livingston, F. E., Whipple, G. C. & George, S. M. (1997), ‘Diffusion of HDO into single-crystal (H<sub>2</sub>O)-O-16 ice multilayers: Comparison with (H<sub>2</sub>O)-O-18’, *Journal of Physical Chemistry B* **101**(32), 6127–6131.
- Lorius, C., Merlivat, L., Jouzel, J. & Pourchet, M. (1979), ‘A 30,000-yr isotope climatic record from Antarctic ice’, *Nature* **280**, 644 – 648.
- Majoube, M. (1970), ‘Fractionation factor of <sup>18</sup>O between water vapour and ice’, *Nature* **226**(1242).
- Maselli, O. J., Fritzsche, D., Layman, L., McConnell, J. R. & Meyer, H. (2013), ‘Comparison of water isotope-ratio determinations using two cavity ring-down instruments and classical mass spectrometry in continuous ice-core analysis’, *Isotopes in Environmental and Health Studies* pp. 1–12.  
**URL:** <http://dx.doi.org/10.1080/10256016.2013.781598>
- Meijer, H. A. J. & Li, W. J. (1998), ‘The use of electrolysis for accurate delta O-17 and delta O-18 isotope measurements in water’, *Isotopes In Environmental And Health Studies* **34**(4), 349–369.
- Merlivat, L. & Jouzel, J. (1979), ‘Global Climatic Interpretation of the Deuterium-Oxygen 18 Relationship for Precipitation’, *Journal of Geophysical Research* **84**(8).
- Merlivat, L. & Nief, G. (1967), ‘Fractionnement Isotopique Lors Des Changements Detat Solide-Vapeur Et Liquide-Vapeur De Leau A Des Temperatures Inferieures A 0 Degrees C’, *Tellus* **19**(1), 122–127.
- Mook, J. (2000), *Environmental Isotopes in the Hydrological Cycle Principles and Applications*, International Atomic Energy Agency.
- Murphy, D. M. & Koop, T. (2006), ‘Review of the vapour pressures of ice and supercooled water for atmospheric applications’, *Q.J.R. Meteorol. Soc.* **131**, 1539–1565.
- NGRIP members (2004), ‘High-resolution record of Northern Hemisphere climate extending into the last interglacial period’, *Nature* **431**(7005), 147–151.
- Oerter, H., Graf, W., Meyer, H. & Wilhelms, F. (2004), ‘The EPICA ice core Droning Maud Land: first results from stable-isotope measurements’, *Ann. Glaciol.* **39**, 307–312.
- Press, W. H., Teukolsky, S. A., Vetterling, W. T. & Flannery, B. P. (2007), *Numerical Recipes: The Art of Scientific Computing*, Cambridge University Press.
- Ramseier, R. O. (1967), ‘Self-diffusion of tritium in natural and synthetic ice monocrystals’, *Journal Of Applied Physics* **38**(6), 2553–2556.
- Rasmussen, S. O., Abbott, P. M., Blunier, T., Bourne, A., Brook, E., Buchardt, S. L., Buizert, C., Chappellaz, J., Clausen, H. B., Cook, E., Dahl-Jensen, D., Davies, S. M., Guillevic, M., Kipfstuhl, S.,



- Laepple, T., Seierstad, I. K., Severinghaus, J., Steffensen, J. P., Stowasser, C., Svensson, A., Vallenga, P., Vinther, B. M., Wilhelms, F. & Winstrup, M. (2013), 'A first chronology for the North Greenland Eemian Ice Drilling (NEEM) ice core', *Climate of the Past* **9**, 2713–2730.
- Rasmussen, S. O., Bigler, M., Blockley, S. P., Blunier, T., Buchardt, S. L., Clausen, H. B., Cvijanovic, I., Dahl-Jensen, D., Johnsen, S. J., Fischer, H., Gkinis, V., Guillevic, M., Hoek, W. Z., Lowe, J. J., Pedro, J. B., Popp, T., Seierstad, I. K., Steffensen, J. P. P., Svensson, A. M., Vallenga, P., Vinther, B. M., Walker, M. J., Wheatley, J. J. & Winstrup, M. (2014), 'A stratigraphic framework for abrupt climatic changes during the last glacial period based on three synchronized greenland ice-core records: refining and extending the intimate event stratigraphy', *Quaternary Science Reviews* **106**, 14–28.
- Schoenemann, S. W., Schauer, A. J. & Steig, E. J. (2013), 'Measurement of SLAP2 and GISP  $\delta^{17}\text{O}$  and proposed VSMOW-SLAP normalization for  $\delta^{17}\text{O}$  and  $^{17}\text{O}_{\text{excess}}$ ', *Rapid Commun. Mass Spectrom.* **27**, 582–590.
- Schwander, J., Sowers, T., Barnola, J.-M., Blunier, T., Fuchs, A. & Malaiz, B. (1997), 'Age scale of the air in the summit ice: Implications for glacial-interglacial temperature change', *Journal of Geophysical Research* **102**(D16), 19,483 –19,493b.
- Schwander, J., Stauffer, B. & Sigg, A. (1988), 'Air mixing in firn and the age of the air at pore close-off', *Annals of Glaciology* pp. 141 –145.
- Severinghaus, J. P. & Brook, E. J. (1999), 'Abrupt climate change at the end of the last glacial period inferred from trapped air in polar ice', *Science* **286**(5441), 930–934.
- Severinghaus, J. P., Sowers, T., Brook, E. J., Alley, R. B. & Bender, M. L. (1998), 'Timing of abrupt climate change at the end of the Younger Dryas interval from thermally fractionated gases in polar ice', *Nature* **391**(6663), 141–146.
- Simonsen, S. B., Johnsen, S. J., Popp, T. J., Vinther, B. M., Gkinis, V. & Steen-Larsen, H. C. (2011), 'Past surface temperatures at the NorthGRIP drill site from the difference in firn diffusion of water isotopes', *Climate of the Past* **7**.
- Steig, E. J., Ding, Q., White, J. W. C., Kttel, M., Rupper, S. B., Neumann, T. A., Neff, P. D., Gallant, A. J. E., Mayewski, P. A., Taylor, K. C., Hoffmann, G., Dixon, D. A., Schoenemann, S., M., M. B., Schneider, D. P., Fudge, T. J., Schauer, A. J., Teel, R. P., Vaughn, B., Burgener, L., Williams, J. & Korotkikh, E. (2013), 'Recent climate and ice-sheet change in West Antarctica compared to the past 2000 years', *Nature Geoscience* **6**.
- Steig, E. J., Gkinis, V., Schauer, A. J., Schoenemann, S. W., Samek, K., Hoffnagle, J., Dennis, K. J. & Tan, S. M. (2014), 'Calibrated high-precision  $^{17}\text{O}$ -excess measurements using cavity ring-down spectroscopy with laser-current-tuned cavity resonance', *Atmos. Meas. Tech.* **7**(8), 2421–2435.

- Svensson, A., Fujita, S., Bigler, M., Braun, M., Dallmayr, R., Gkinis, V., Goto-Azuma, K., Hirabayashi, M., Kawamura, K., Kipfstuhl, S., Kjr, H. A., Popp, T., Simonsen, M., Steffensen, J. P., Vallelonga, P. & Vinther, B. M. (2015), 'On the occurrence of annual layers in Dome Fuji ice core early Holocene Ice', *Climate of the Past* **11**, 1127–1137.
- van der Wel, G., Fischer, H., Oerter, H., Meyer, H. & Meijer, H. A. J. (2015), 'Estimation and calibration of the water isotope differential diffusion length in ice core records', *The Cryosphere* **9**(4), 1601–1616.
- Vaughn, B. H., White, J. W. C., Delmotte, M., Troler, M., Cattani, O. & Stievenard, M. (1998), 'An automated system for hydrogen isotope analysis of water', *Chemical Geology* **152**(3-4), 309–319.
- Veres, D., Bazin, L., Landais, A., Kele, H. T. M., Lemieux-Dudon, B. B., Parrenin, F., Martinerie, P., Blayo, E., Blunier, T., Capron, E., Chappellaz, J., Rasmussen, S. O., Severi, M., Svensson, A., Vinther, B. & Wolff, E. W. (2013), 'The Antarctic ice core chronology (AICC2012): an optimized multi-parameter and multi-site dating approach for the last 120 thousand years', *Climate of the Past* **9**.
- Vinther, B. M., Buchardt, S. L., Clausen, H. B., Dahl-Jensen, D., Johnsen, S. J., Fisher, D. A., Koerner, R. M., Raynaud, D., Lipenkov, V., Andersen, K. K., Blunier, T., Rasmussen, S. O., Steffensen, J. P. & Svensson, A. M. (2009), 'Holocene thinning of the Greenland ice sheet', *Nature* **461**.
- Vinther, B. M., Clausen, H. B., Johnsen, S. J., Rasmussen, S. O., Andersen, K. K., Buchardt, S. L., Dahl-Jensen, D., Seierstad, I. K., Siggaard-Andersen, M. L., Steffensen, J. P., Svensson, A., Olsen, J. & Heinemeier, J. (2006), 'A synchronized dating of three greenland ice cores throughout the holocene', *Journal Of Geophysical Research-Atmospheres* **111**(D13102).
- Watanabe, O., Shoji, H., Satow, K and, M. H., Fujii, Y., Narita, H. & S., A. (2003), 'Dating of the Dome Fuji, Antarctica deep ice core', *Mem. Natl Inst. Polar Res., Spec. Issue* **57**, 25–37.
- Whillans, I. M. & Grootes, P. M. (1985), 'Isotopic diffusion in cold snow and firn', *Journal of Geophysical Research - Atmospheres* **90**, 3910–3918.